Paleoceanography and Paleoclimatology

RESEARCH ARTICLE
10.1029/2024PA004887

Intense Changes in the Main Source of Organic Carbon to the Gulf Coastal Plain Following the Cretaceous-Paleogene Boundary

C. Sosa-Montes de Oca[1], J. D. Witts[1,2], C. M. Lowery[3], L. E. Kearns[3], M. P. Garb[4], J. Naujokaityte[5], C. E. Myers[5], N. H. Landman[6], and R. D. Pancost[1]

[1]Organic Geochemistry Unit, The Cabot Institute for the Environment, Bristol Palaeobiology Research Group, School of Earth Sciences, School of Chemistry, University of Bristol, Bristol, UK, [2]The Natural History Museum, London, UK, [3]University of Texas Institute for Geophysics, University of Texas at Austin, Austin, TX, USA, [4]Department of Earth and Environmental Sciences, Brooklyn College, Brooklyn, NY, USA, [5]Department of Earth and Planetary Sciences, University of New Mexico, Albuquerque, NM, USA, [6]Division of Paleontology (Invertebrates), American Museum of Natural History, New York, NY, USA

Abstract To explore both environmental change and the response of non-fossilizing phytoplankton across the Cretaceous-Paleogene (K-Pg) boundary mass extinction event, we determined changes in organic matter (OM) sources using a range of apolar (*n*-alkanes, acyclic isoprenoids, steranes, and hopanes) and polar (BIT index) biomarkers. We analyzed two K-Pg proximal sections, located in the Mississippi Embayment, Gulf Coastal Plain (USA), covering ~300 kyrs prior to and ~3 myrs after the K-Pg event. The OM abundance and composition changed dramatically across the boundary. The post-impact ejecta layer and burrowed unit are characterized by an increase in the mass accumulation rate (MAR) of plant and soil biomarkers, including high-molecular-weight *n*-alkanes and C_{29} steranes as well as the BIT index, related to an erosive period which transported terrestrial OM to the ocean in the aftermath of the impact event. At the same time, MARs of putative aquatic biomarkers decrease (low-molecular-weight *n*-alkanes, C_{27} steranes and pristane and phytane), which suggests a collapse of the marine phytoplankton community. The increase of terrestrial OM to the ocean, during the first 280 kyrs after the Chicxulub impact event, is a combination of reworked kerogen, soil and some plant material. Crucially, within the latter part of this erosion period, only ~160 kyrs after the K-Pg do biomarkers return to distributions similar to those in the upper Cretaceous, although not to pre-impact MARs. Thus, our results suggest a long-term interval for the full sedimentary and ecological recovery of the non-fossilizing phytoplankton community after this event.

Plain Language Summary The Cretaceous-Paleogene (K-Pg) boundary coincides with the latest of the five major mass extinctions in Earth's history. Determining the nature of the associated rapid environmental change and biotic recovery is critical for knowing the cause and effects of this key event and contributes to our understanding of the ongoing biodiversity crisis. We analyzed biomarkers (molecular fossils) in two K-Pg sections in the Gulf Coastal Plain (USA) near the impact site, covering ~300,000 years prior to, and ~3,000,000 years after the K-Pg event. The organic matter (OM) abundance and composition changed dramatically after the impact event. In particular, an increase in the concentration of plant and soil biomarkers occurred in the first 280,000 years after the impact and is attributed to an erosive period which transported OM from the land to the ocean. At the same time, the concentrations of marine algal biomarkers decrease, suggesting a collapse of the marine algal community. About 160,000 after the K-Pg event, marine biomarkers return to distributions similar to those pre-impact. This suggests an initial recovery of algal communities on the Gulf Coastal Plain, although they never recover to pre-impact abundances during the studied interval (~3,000,000 after impact).

Key Points:

- Intense erosive regime after the K-Pg boundary, coincident with collapse of the marine phytoplankton community on the Gulf Coastal Plain
- Initial recovery of non-fossilizing algal communities started ~160 kyr after the K-Pg event although with lower mass accumulation rates than pre-impact
- Sedimentary conditions never return to their pre-impact state, suggesting a long-term perturbation to the system

Supporting Information:

Supporting Information may be found in the online version of this article.

Correspondence to:

C. Sosa-Montes de Oca,
claudia.sosamontesdeoca@bristol.ac.uk

Citation:

Sosa-Montes de Oca, C., Witts, J. D., Lowery, C. M., Kearns, L. E., Garb, M. P., Naujokaityte, J., et al. (2024). Intense changes in the main source of organic carbon to the Gulf Coastal Plain following the Cretaceous-Paleogene boundary. *Paleoceanography and Paleoclimatology*, *39*, e2024PA004887. https://doi.org/10.1029/2024PA004887

Received 29 FEB 2024
Accepted 31 JUL 2024

Author Contributions:

Conceptualization: C. Sosa-Montes de Oca, J. D. Witts, R. D. Pancost
Formal analysis: C. M. Lowery, L. E. Kearns
Funding acquisition: C. Sosa-Montes de Oca, R. D. Pancost
Investigation: C. Sosa-Montes de Oca, J. D. Witts, C. M. Lowery, M. P. Garb, J. Naujokaityte, C. E. Myers, N. H. Landman, R. D. Pancost
Methodology: C. Sosa-Montes de Oca, R. D. Pancost
Resources: C. Sosa-Montes de Oca, J. D. Witts
Supervision: R. D. Pancost

1. Introduction

The Cretaceous-Paleogene (K-Pg) boundary, dated 66.00 Ma (Sprain et al., 2018), coincides with the most recent of the five largest mass extinction events in Earth history (D'Hondt, 2005; Raup & Sepkoski, 1982). It is broadly accepted that this mass extinction was triggered by a meteorite impact (Alegret et al., 2022; Alvarez et al., 1980; Hull et al., 2020; Pälike, 2013; Schulte et al., 2010) associated with the Chicxulub structure on the Yucatan Platform in the southern Gulf of Mexico (Hildebrand et al., 1991; Swisher et al., 1992), but the role of additional

Writing – original draft: C. Sosa-Montes de Oca
Writing – review & editing: C. Sosa-Montes de Oca, J. D. Witts, C. M. Lowery, L. E. Kearns, M. P. Garb, J. Naujokaityte, C. E. Myers, N. H. Landman, R. D. Pancost

environmental perturbations caused by Deccan Traps volcanism are still debated (Gilabert et al., 2021; Renne et al., 2015; Schoene et al., 2015, 2019). The extinction of primary producers at the K-Pg boundary and their subsequent recovery has been the subject of much recent interest (Sosa-Montes de Oca et al., 2013, 2018a, 2018b, 2020, 2021, 2023; Bralower et al., 2020; Gulick et al., 2019; Lowery, Bralower, et al., 2018, Lowery et al., 2020; Rodríguez-Tovar et al., 2020; Schaefer et al., 2020). Within primary producers, calcareous nannoplankton suffered very high extinction rates ~93% at this event (e.g., Bown et al., 2004; Lowery et al., 2020); haptophyte algae (coccolithophores) were almost entirely eradicated (>90% species extinction) (Bown et al., 2004). This differed from the fate of at least some non-calcifying species, such as dinoflagellates, which do not appear to suffer major extinction at this event (e.g., Brinkhuis & Leereveld, 1988; McLachlan & Pospelova, 2021; Vellekoop et al., 2015). However, it remains unclear how the microbial and non-fossilizing phytoplankton communities were affected. In this paper we aim to improve our understanding of the non-fossilizing phytoplankton and bacteria response to the K-Pg mass extinction through changes in lipid biomarker assemblages and sources of organic matter (OM).

The Chicxulub impact event was responsible for a range of global environmental perturbations including nitric and sulfuric acid rain (Senel et al., 2023); input of soot, dust and aerosols to the atmosphere; destruction of the stratospheric ozone layer (Kring, 2007); and an input of greenhouse gases (e.g., Kring, 2007; Morgan et al., 2022 and references therein; Senel et al., 2023). Some of these initial disturbances also led to secondary effects such as an increase in ocean acidification (e.g., Alegret & Thomas, 2005; Alegret et al., 2012; Henehan et al., 2019; Junium et al., 2022; Ohno et al., 2014; Peryt et al., 2002; Witts et al., 2018), a decrease in sunlight (Alvarez et al., 1980; Morgan et al., 1997), and complex temperature changes (Galeotti et al., 2004; Kaiho et al., 2016; MacLeod et al., 2018; O'Connor et al., 2023; Scasso et al., 2020; Taylor et al., 2018; Vellekoop et al., 2014, 2015). Such perturbations sharply transformed depositional and ecological conditions worldwide (Alegret & Thomas, 2005; Peryt et al., 2002). In addition, some studies suggest that the late Maastrichtian to early Paleogene was marked by relatively long-term changes in relative sea level (Adatte et al., 2002; Habib et al., 1992; Kominz et al., 2008; Macleod & Keller, 1991; Miller et al., 2005; Schulte et al., 2006). Evidence for a eustatic regression has been suggested at several K-Pg sections worldwide (Scasso et al., 2020; Vellekoop et al., 2017; Zhang et al., 2018). That could be responsible for an increase of both terrestrial and reworked marine OM input to the ocean, as has been previously detected in several marine sections (regardless of whether they were distal or proximal, shallow or deep) above the boundary layer (Mizukami et al., 2013, 2014; Scasso et al., 2020; Sepúlveda et al., 2019; Sosa-Montes de Oca et al., 2021, 2023). In addition to global consequences, locales close to the Chicxulub impact structure ("very proximal" and "proximal" sites, e.g.; Schulte et al., 2010), were particularly affected by a range of local effects, such as tsunamis, marine landslides, and fires (Kaiho et al., 2016; Kring, 2007; Lyons et al., 2020; Morgan et al., 2013; Sanford et al., 2016; Santa Catharina et al., 2022). This work clearly shows that the nature and thickness of the stratigraphic layers related to the impact itself differ with distance from the Chicxulub impact crater (Schulte et al., 2010). While distal K-Pg outcrops are ideal for understanding the global environmental consequences of the impact, proximal marine deposits provide information about the immediate physical effects of the impact and associated environmental changes. Although these proximal sites were more affected by the destructive forces of the impact, being highly disturbed and/or reworked, they also contain expanded early Paleogene records (Smit, 1999), and are ideal for high resolution analyses.

Biomarkers preserved in sedimentary sequences and structurally linked to specific biological sources (e.g., T. I. Eglinton & Eglinton, 2008; Peters et al., 2005) are powerful tools for exploring biotic changes and OM sources (Xie et al., 2010). Moreover, biomarker degradation and alteration is governed by environmental conditions, such that they can also used to reconstruct paleoenvironmental conditions (e.g., T. I. Eglinton & Eglinton, 2008; Peters et al., 2005). Although limited, there have now been several biomarker studies on the biotic response and recovery after the K-Pg boundary in distal sections (Bralower et al., 2020; Rosenberg et al., 2021; Sepúlveda et al., 2009; Sosa-Montes de Oca et al., 2021, 2023; Taylor et al., 2018). There has also been biomarker work focused on the biotic response within the Chicxulub structure (Mizukami et al., 2014; Schaefer et al., 2020), and recently, in intermediate terrestrial sites (O'Connor et al., 2023). Few studies have focused on biomarkers at proximal sites (Mizukami et al., 2014; Vellekoop et al., 2014, 2016). As the K-Pg boundary was a global event, filling this gap provides clarity regarding changes in both the response of non-fossilizing phytoplankton as well as environmental conditions through this event.

Here, we present biomarker analyses through a ~5.7 m composite interval from a proximal K-Pg boundary section in the Mississippi Embayment, Gulf Coastal Plain (USA). Our composite interval provides a nearly

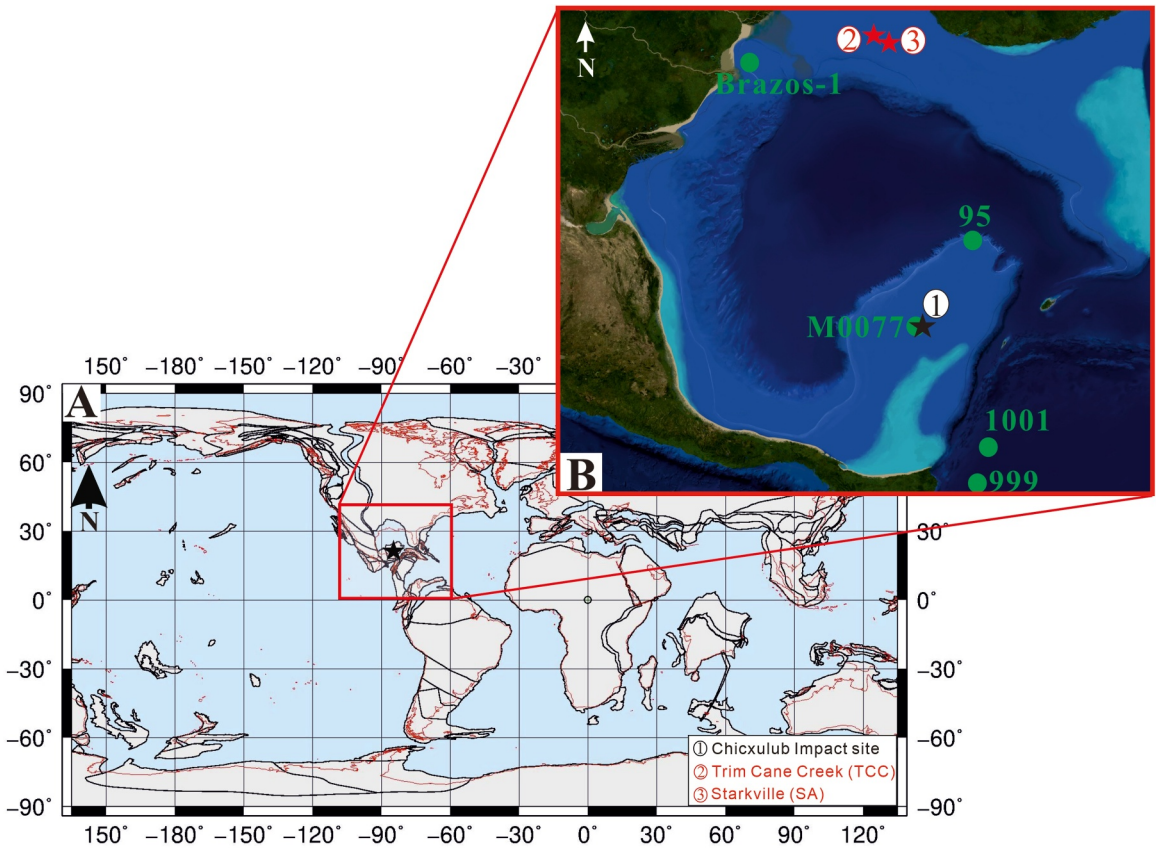

Figure 1. Location of the studied proximal K-Pg boundary sections. (a) Paleogeographic reconstruction at the time of the K-Pg boundary (66.00 Ma) (https://www.odsn.de/odsn/services/paleomap/adv_map.html). The red line shows the present-day shoreline. The black star shows the Chicxulub impact locate. (b) Paleogeographic location of the Trim Cane Creek and Starkville (SA) sections, both located in the Mississippi Embayment, Gulf Coastal Plain (USA). Map modified from Victor Leshyk for the Lunar and Planetary Science Institute and based on (Snedden et al., 2024). In green color are others K-Pg sections (e.g., IODP Site M0077 in the Chicxulub crater, DSDP Site 95 in the Gulf of Mexico, ODP Sites 999 and 1001 in the Caribbean and the mid-shelf Brazos-1 section (Texas)).

complete record of events at the time of the K-Pg boundary (Irizarry et al., 2023; Lowery, Leckie, et al., 2018; Naujokaitytė et al., 2021). We examine the abundance and distribution of apolar biomarkers, including *n*-alkanes (mixed sources, e.g., terrestrial, and marine sources), acyclic isoprenoids (pristane and phytane; algal chlorophyll origin), steranes (eukaryotes mixed sources) and hopanes (bacteria), and polar biomarkers such as glycerol dialkyl glycerol tetraether lipids (GDGTs) that have archeal and bacterial origins. We identify and discuss the implications of a marked increase in terrestrially derived biomarkers (i.e., high-molecular-weight *n*-alkanes, C_{29} steranes, and BIT index) that coincides with a decrease in marine derived biomarkers (i.e., low-molecular-weight *n*-alkanes, C_{27} steranes and, pristane and phytane) in horizons immediately above the K-Pg boundary. Only ∼160 kyrs after the impact (Clayton Fm.) do biomarker distributions, including sterane assemblages and the presence of pristane and phytane, return to pre-K-Pg boundary conditions, suggesting the partial recovery of non-fossilizing algal communities. However, persistently low $CaCO_3$ and biomarker mass accumulation rates (MARs) suggest that the depositional system still had not fully recovered ∼3 Myr later.

2. Geological Setting

Latest Cretaceous sediments in the Mississippi Embayment (Figure 1) were deposited in estuarine to outer shelf settings (∼50–150 m water depth) (Larina et al., 2016) located ∼1,500 km from the Chicxulub impact site (Schulte et al., 2010). For this study we focused on samples from two outcrops/three localities: Trim Cane Creek (TCC; *American Museum of Natural History (AMNH) localities 3944a and 3944b*) and Starkville (SA; *AMNH locality 3525*), approximately ∼6.5 km apart in the Mississippi Embayment, Gulf Coastal Plain (USA) to obtain a complete composite record across the K-Pg boundary (Figure 2). We describe the localities in this section,

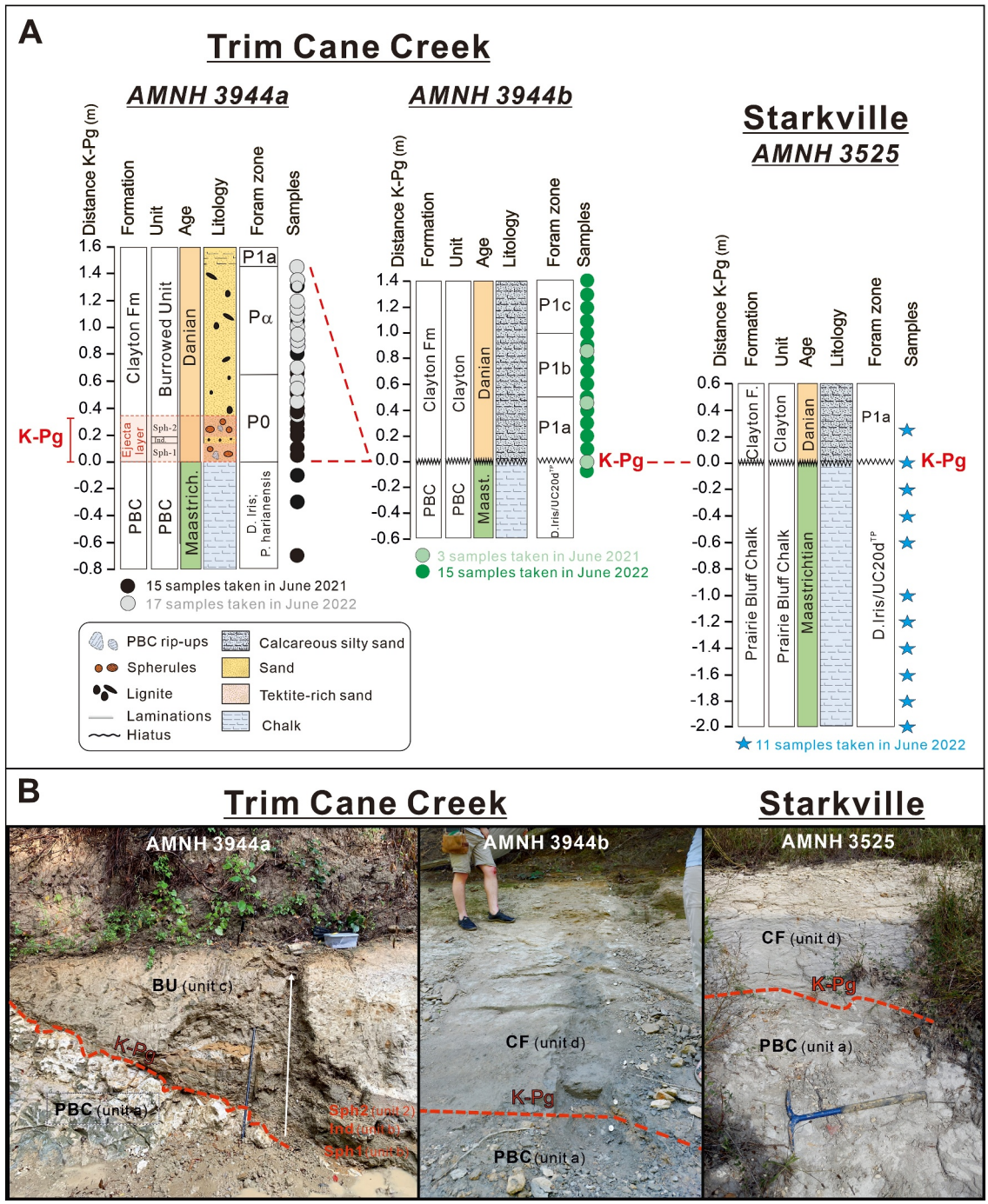

Figure 2. (a) Stratigraphic columns of the Trim Cane Creek (*AMNH* localities *3944a* and *3944b*) and Starkville (SA; *AMNH* locality *3525*) outcrops. (b) Photographs from each outcrops/localities on the field.

including their location, lithology and the relevant Formations; we then present new biostratigraphic results in Section 4.1 that allow a more thorough view of the completeness of the composite section and the age model.

2.1. Starkville (*AMNH* Locality *3525*): (33.455444°N, 88.849444°W)

The sampled section at Starkville (Figure 2) consists of 7.9 m of Maastrichtian Prairie Bluff Chalk overlain by the lowermost Danian Clayton Formation. The Prairie Bluff Chalk is a heavily bioturbated (burrows 30–40 cm),

slightly micaceous, silty marl alternating with indurated, gray to white, slightly micaceous bioturbated chalk. Chalk and marl couplets are conspicuous, typically 50–60 cm thick, and probably represent primary depositional features (Naujokaitytė et al., 2021). The upper 3.5 m of the Prairie Bluff Chalk is abundantly fossiliferous, with molluscan macrofossils preserved as internal molds. The contact with the overlying Clayton Formation marks the K-Pg boundary. This contact is undulating and burrowed extensively by *Thalassinoides*, which pipes down material into the Prairie Bluff Chalk for up to ∼1 m. The Clayton Formation itself is a 30 cm-thick silty, micaceous, marly fine sand. In June 2022, we sampled the upper 2.00 m of the Prairie Bluff Chalk every 20 cm and took a single sample from the basal Clayton Formation 25 cm above the K-Pg boundary (11 samples in total).

2.2. Trim Cane Creek (*AMNH* Localities *3944a* and *3944b*): (33.469611°N, 88.908306°W)

Trim Cane Creek (Figure 2) lies 6.5 km west of the town of Starkville, MS. We sampled two localities, both on private land along the creek with permission from the landowner. The first is *AMNH 3944b,* where the K-Pg boundary is again marked by the contact between the uppermost Maastrichtian Prairie Bluff Chalk and the lowermost Danian Clayton Formation. This contact is primarily an undulating unconformable surface heavily bioturbated with *Thalassinoides* burrows which penetrate almost a meter into the Prairie Bluff Chalk, very similar to the Starkville locality (Larina et al., 2016; Naujokaitytė et al., 2021). Here the Prairie Bluff Chalk is finely bioturbated with abundant macrofossils, including the ammonite *Discoscaphites iris*, indicative of the upper Maastrichtian *D. iris* Zone. The Clayton Formation above this unconformable surface comprises 1.5 m of dark silty, micaceous, marly chalk with occasional large burrows. We sampled the Clayton Formation in June 2021 (3 spot samples) and then at 10 cm resolution in June 2022 (15 samples).

The second locality sampled at TCC is *AMNH 3944a*, approximately ∼500 m to the NE of *AMNH 3944b*. Here, and elsewhere along TCC, the upper surface of the Prairie Bluff Chalk is overlain along a sharp basal contact by complex channel deposits. These basal Clayton Formation channels are associated with faults and appear to represent down-dropped blocks. We sampled the upper Prairie Bluff Chalk at 70, 30, and 10 cm below the K-Pg, in June 2021 (three samples in total). We sampled one of these channels in detail two times, first in June 2021 and later in June 2022. The sampled interval contains two ∼12–15 cm-thick ejecta-rich beds at the base, containing abundant altered impact spherules and tektites along with large (1–5 cm-sized) rip-up clasts of Prairie Bluff Chalk and reworked Cretaceous fossils (most commonly baculitid and scaphitid ammonites and crassatellid bivalves) (Figure 2). In between the two spherule-rich beds is an 8 cm-thick micaceous, lignitic, quartz silty sand with scattered single burrows 2 cm in diameter. In June 2021, we took two samples of each of the spherule beds and one in the indurated bed (five samples in total). Conformably overlying the spherule beds is a heavily bioturbated unit totally devoid of spherules referred to as the "burrowed unit." The burrowed unit is lignite-rich and carbonate-poor, consisting of 1.25 m of micaceous, muddy fine sands which become more silt-rich toward the top of the succession, resembling the "background" Clayton Formation. These sediments are intensely bioturbated, with some individual large *Thalassinoides*-type burrows traceable for up to 85 cm vertically through the unit. We analyzed two sets of samples from the burrowed unit: one set collected at 20 cm resolution, in June 2021 (seven samples in total), and a second set, where the basal 60 cm of the burrowed unit were sampled at 10 cm resolution and the upper 60 cm at 5 cm resolution, in June 2022 (17 samples in total).

We built a ∼5.7 m thick composite section (Figure 3), which includes all three localities from the two sites described above and shows a complete and continuous K-Pg interval, including 2.7 m of uppermost Cretaceous (Prairie Bluff Chalk Fm.—unit a) and 3.0 m of Paleogene sediment (Clayton Fm); the latter includes 0.35 m of an ejecta-rich layer (unit b), overlain by ∼1.25 m of highly bioturbated, muddy lignitic quartz sand (burrowed unit—unit c) and 1.4 m of marly siltstone (Clayton Fm proper—unit d) (Figure 3).

The ∼5.7 m thick composite section was sampled for biomarker analysis at a resolution of 20 cm for the Cretaceous and between 10 and 5 cm resolution for the Paleogene (Figure 2). Because only ∼70 cm of the uppermost Prairie Bluff Chalk Fm (unit a) are exposed at TCC, most of the samples from this formation came from SA (*AMNH 3525*). Similarly, because both SA and *AMNH 3944b* contain a more extensive hiatus at the K-Pg boundary and units b and c are not present, these were sampled only at *AMNH 3944b* (Figure 3). In total, at both sections (three localities) 61 samples were taken for biomarker analyses and 16 samples for inorganic geochemistry, Total Organic Carbon (TOC) and isotope analysis ($\delta^{13}C_{TOC}$ and $\delta^{13}C_{Carb}$).

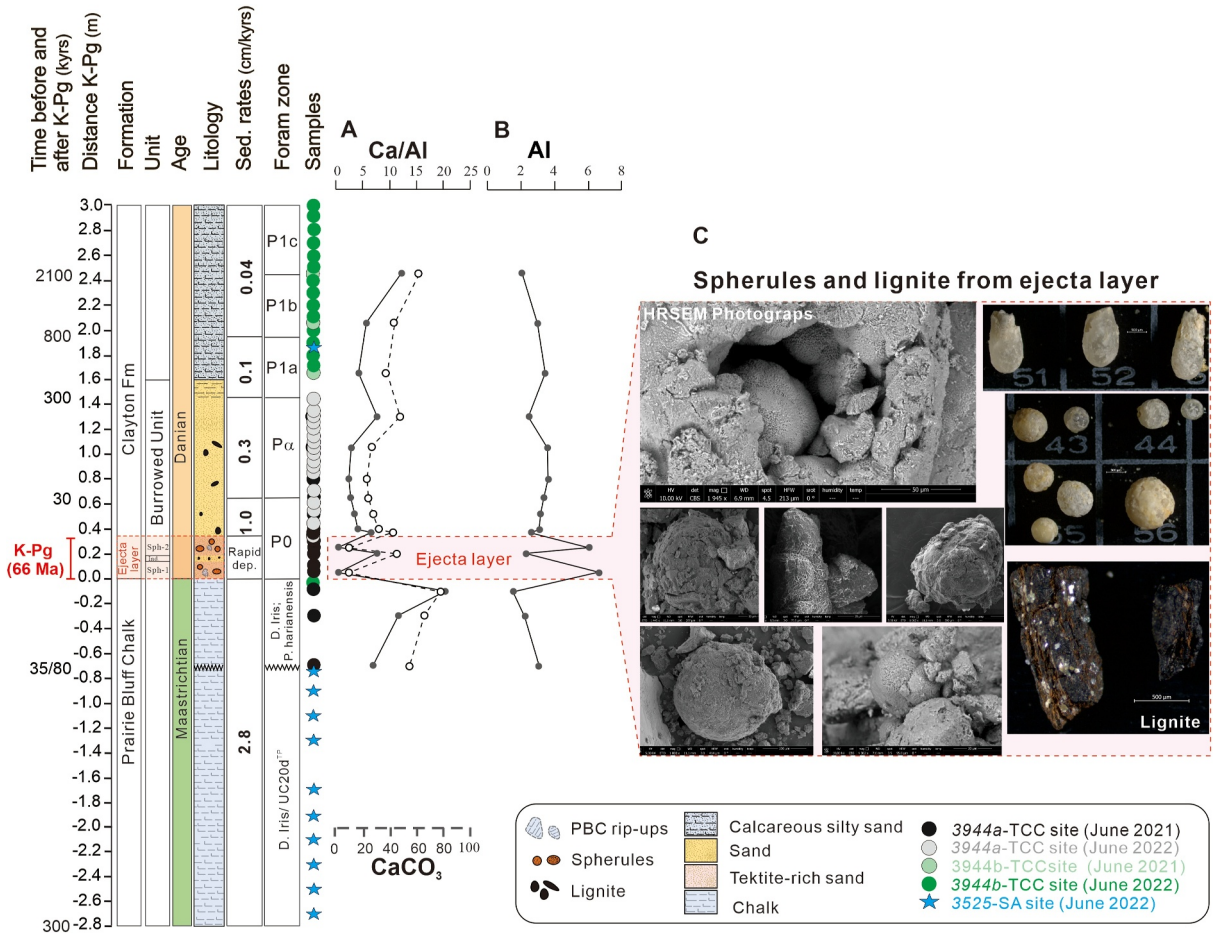

Figure 3. Stratigraphic column of our composite K-Pg boundary section. Samples from the Trim Cane Creek (TCC, *AMNH 3944a* and *AMNH 3944b*) section are in circles; the TCC section was sampled in two different sites, *AMNH 3944a* (first in June 2021 [black color] and a high-resolution sampling in June 2022 [gray color]) and *AMNH 3944b* (first time in June 2021 [light green color] and second time for a high-resolution sampling in June 2022 [green color]). Samples from the Starkville (SA; *AMNH 3525*) section are in blue stars and were collected in June 2022. The ∼5.7 m thick composite profile comprises 2.7 m of uppermost Cretaceous (Prairie Bluff Chalk Fm. unit a) and 3.0 m of Paleogene sediment; the latter includes an ejecta-rich layer (unit b), which contains two 10–15 cm-thick spherule-rich sandstone beds, overlain by 1.25 m of highly bioturbated, muddy lignite quartz sand (burrowed unit; unit c) and 1.40 m of marly siltstone (Clayton Fm, unit d). (a) Ca/Al ratio and $CaCO_3$ content (calculated from Ca * 2.5, %) at TCC- *AMNH 3944a* section. (b) Al (%) profile at TCC-*AMNH 3944a* section. (c) Photographs of the impact spherules and lignite particle from the TCC-*AMNH 3944a* section at the ejecta layer.

3. Methods

3.1. Micropaleontological Analysis

Micropaleontological analysis was carried out on 12 samples from TCC at a roughly 20 cm resolution and three samples from Starkville, one from each facies of the Clayton Formation. Samples were broken up with a mortar and pestle into ∼1 cm chunks, soaked for at least 24 hr in a solution of peroxide and borax to aid disaggregation, and then washed over a 45 μm sieve. The sieved residue was then dried overnight in an oven and analyzed under a Zeiss Discovery V8 microscope for the presence/absence of biostratigraphically significant taxa. Planktic foraminifera zones follow the (Wade et al., 2011) update of the Paleocene biozonation scheme of Berggren and Pearson (2005) with ages calibrated to the timescale of Speijer et al. (2020).

3.2. Total Organic Carbon (TOC), Carbon Isotope Analyses and Inorganic Geochemistry

For determination of TOC, carbon isotope analyses ($\delta^{13}C_{TOC}$ and $\delta^{13}C_{Carb}$), and major and trace elements (inorganic geochemistry), 16 samples were analyzed in the TCC section from 0.7 m below to 2.05 m above the K-Pg boundary. This includes three samples from Prairie Bluff Chalk (unit a; *AMNH 3944a*), three samples from the

ejecta layer (unit b; *AMNH 3944a*), seven samples from the 1.0 m-thick burrowed unit (unit c, *AMNH 3944a*); and three samples from the 1.4 m-thick Clayton Fm (unit d; *AMNH 3944b*).

The TOC and bulk OM $\delta^{13}C$ values ($\delta^{13}C_{TOC}$) were analyzed in the Stable Isotope Laboratory (SIDI) at the Universidad Autónoma de Madrid (Spain). While $\delta^{13}C_{Carb}$ and major and trace elements content were analyzed at Centro de Instrumentación Científica (CIC) from Universidad de Granada (Spain).

The TOC content was calculated using a SHIMADZU TOC-VCSH (Continuous automatic high-sensitivity). First, samples were treated with hydrogen chloride (HCl at 1.5 M) for 2 hr to remove carbonates, washed, and then dried at 60°C. TOC concentration was determined by subtracting the inorganic carbon (IC) from the total carbon (TC) content in each sample. Once IC was removed, all samples were weighed (between 0.012 and 0.030 g, depending on the quantity of TC) and then were analyzed with an elemental analyzer, a Carlo Erba 1108 coupled to a Isotope Ratio Mass Spectrometer (IRMS) VG Isochrom, in continuous flow mode for bulk OM isotopic ($\delta^{13}C_{TOC}$) determination. The reference material used for $\delta^{13}C$ analysis was IA-R001 [$\delta^{13}C_{V\text{-}PDB} = -26.43‰$], with a precision better than 0.08‰. Results are expressed in the common δ-notation in per mil (‰) relative to the V-PDB standard. For determination of bulk IC isotopic values ($\delta^{13}C_{carb}$), all samples were treated with phosphoric acid (H_3PO_4 at 103%) using a VG Isocarb system thermostatized at 90°C. The liberated CO_2 was analyzed with an Isotope Ratio Mass Spectrometer (IRMS) VG Prism II. The international carbonate standard NBS-19 (National Bureau of Standards; $\delta^{13}C = 1.95‰$ and $\delta^{18}O = -2.20‰$) was used to calibrate to Vienna Pee Dee Belemnite (VPDB), with an average precision of 0.03‰ for $\delta^{13}C_{carb}$ and 0.05‰ for $\delta^{18}O$ analyses.

For inorganic analyses, both major and trace elements, all samples were crushed in an agate mortar and digested with nitric acid (HNO_3) and hydrofluoric acid (HF). Trace element concentrations were determined using Inductively Coupled Plasma-Mass Spectrometry (NEXION 300D; ICP-MS). Results were calibrated using blanks and international standards, with analytical precision better than ±2% for 50 ppm elemental concentrations and ±5% for 5 ppm elemental concentrations. Major element concentration (Al, Ca, Fe, K, Ti, and Mg) was measured in the same sample solutions using an Inductively Coupled Plasma-Optical Emission Spectroscope (Perkin-Elmer Optima 8300; ICP-OES) with a Rh anode X-ray tube. Blanks and international standards were used for quality control and the analytical precision was better than ±2.8% and 1.9% for 50 ppm elemental concentrations of Al and Ca, respectively; better than ±0.5% for 20 ppm elemental concentrations of Fe; better than ±0.4% for 5 ppm elemental concentrations of K; and better than ±1.5% for 2.5 ppm elemental concentrations of Mg. Through the K-Pg interval, large shifts in carbonate content occur, impacting most element distributions. To study elemental variability without this carbonate dilution effect, we followed the standard practice of utilizing Al-normalized concentrations (Calvert & Pedersen, 1993; De Lange et al., 1987; Morford & Emerson, 1999; Tribovillard et al., 2006; Van der Weijden, 2002).

3.3. Biomarker Analysis

Sixty one samples were analyzed across both sections at TCC (localities *AMNH 3944a and 3944b*) and SA (locality *AMNH 3525*), including 14 samples from Prairie Bluff Chalk (unit a), 5 samples from the ejecta layer (unit b), 25 samples from the burrowed unit (unit c); and 17 samples from Clayton Fm (unit d). First, ∼30 g of sediment was freeze-dried, then powdered using a steel ball mill (MM400) and extracted via a Soxhlet apparatus for 48 hr using dichloromethane (DCM)/methanol (MeOH) (2:1 v/v). Then, total lipid extracts were separated into two fractions using a column packed with activated silica by elution with hexane/DCM (9:1 v/v; apolar fraction) and DCM/MeOH (1:2 v/v; polar fraction). Finally, all fractions were evaporated to dryness under a steady flow of nitrogen.

Individual organic compounds (or their derivatives) amenable to Gas Chromatography (GC) were identified in apolar and polar fractions, and quantified relative to internal standards (5α-androstane, apolar fraction) using GC and GC-Mass Spectrometry (GC-MS) for apolar fractions and High Performance Liquid Chromatography/Atmospheric Pressure Chemical Ionization-Mass Spectrometry (HPLC/APCI-MS) for GDGT characterization (Hopmans et al., 2004).

GC analyses were performed on a CarloErba Gas Chromatograph equipped with a flame ionization detector and fitted with a Chrompack fused silica capillary column (50 m × 0.32 mm interior diameter) coated with a CP Sil-5CB stationary phase (dimethylpolysiloxane equivalent, 0.12 μm film thickness). GC-MS analysis was performed on a Thermoquest Finnigan Trace Gas Chromatograph interfaced with a Thermoquest Finnigan Trace Mass

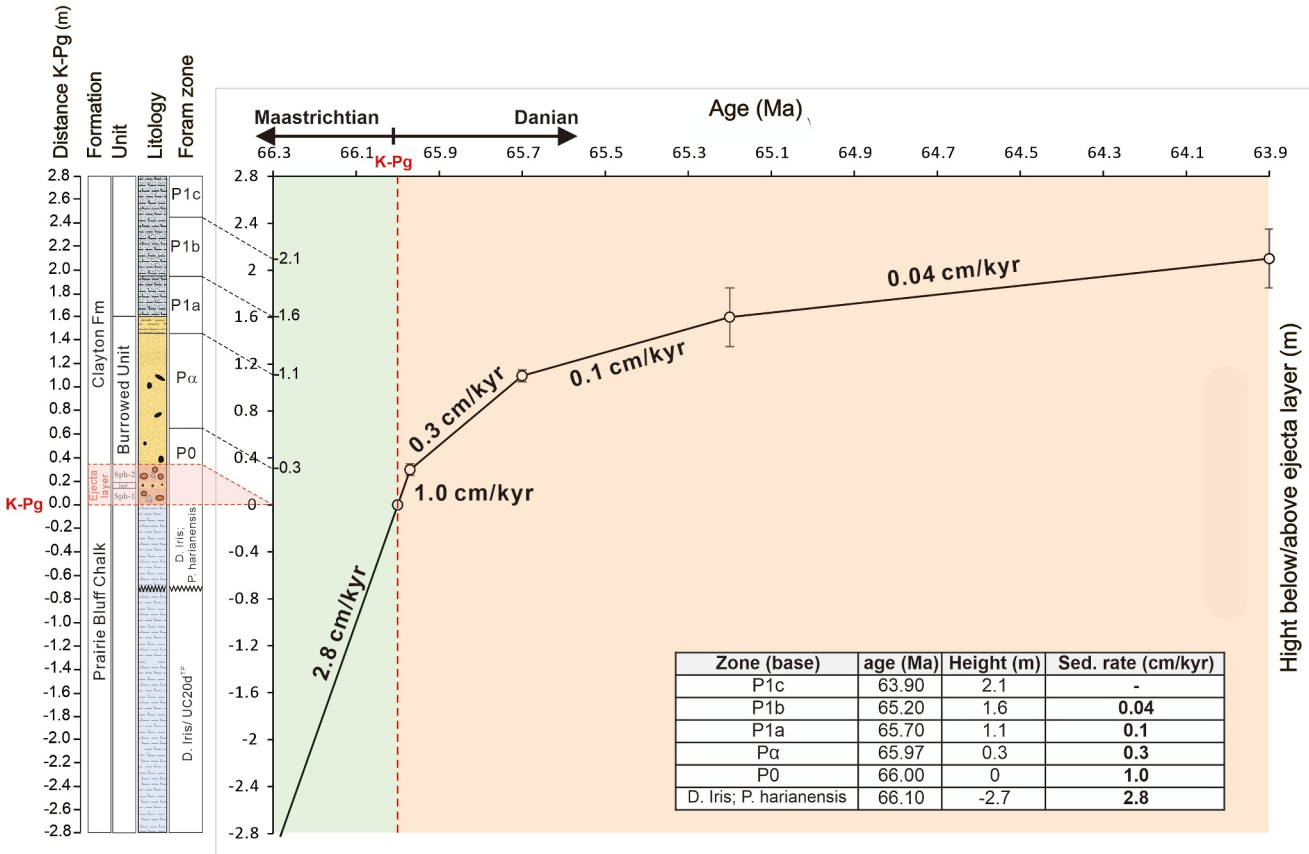

Zone (base)	age (Ma)	Height (m)	Sed. rate (cm/kyr)
P1c	63.90	2.1	-
P1b	65.20	1.6	**0.04**
P1a	65.70	1.1	**0.1**
Pα	65.97	0.3	**0.3**
P0	66.00	0	**1.0**
D. Iris; P. harianensis	66.10	-2.7	**2.8**

Figure 4. Age-depth model plot for our K-Pg composite section based on ammonites and planktonic foraminiferal biozonation. Vertical error bars show depth error in the placement of the datum (i.e., the spacing between samples). Sedimentation rates are shown next to segments of the age model line. For lithology, see caption in Figure 3.

Spectrometer operating with an electron ionization source at 70 eV and scanning over *m/z* ranges of 50–850 Da. The GC was fitted with a fused silica capillary column (50 m × 0.32 mm i.d.) coated with a ZB1 stationary phase (dimethylpolysiloxane equivalent, 0.12 µm film thickness). For both GC and GC-MS, 1 µl of sample was injected at 70°C using an on-column injector. The temperature was increased to 130°C with an initial ramp of 20°C/min, then to 300°C at 4°C/min, followed by an isothermal hold for 20 min. All concentration results are semi-quantitative, with peak areas determined from appropriate mass chromatograms (*n*-alkanes *m/z* 71; hopanes *m/z* 191; steranes *m/z* 217 + 218) and normalized to the internal standard and amount extracted; due to varying response factors, these were not converted into absolute concentrations and we instead normalize the data set to the sample with the highest concentration or MAR as relevant (see below at 3.4).

Analysis of GDGT relative abundances uses HPLC/APCI-MS to separate and detect GDGTs (Hopmans et al., 2004). The most widely adopted current analytical method (based on Schouten et al., 2007) uses a cyano column for chromatographic separation of GDGTs and selected ion monitoring for quantification of GDGT $[M + H]^+$ ions.

3.4. Mass Accumulation Rates

Given the changes in lithology as well as likely changes in sedimentation rates across our section, we calculated MARs (µg/cm^2/kyr) to examine variations in OM input in relation to the time of deposition for different apolar and polar biomarkers. The MAR was obtained by multiplying the concentration (µg/g Dry Weight) of each biomarker (*n*-alkanes, hopanes, steranes, pristane + phytane and GDGTs) by the sedimentation rates (cm^2/kyrs) calculated in each foraminiferal biozone (Figure 4). Because concentrations are semi-quantitative, as discussed above, we then normalized MARs for each compound or class to the sample with the highest value which is set as MAR = 1.

4. Results

4.1. Age Model

The age of the Prairie Bluff Chalk at the Starkville locality is constrained by calcareous nannofossil and ammonite biostratigraphy, and cyclostratigraphy (Naujokaitytė et al., 2021) (Figure 4). The upper 3 m of the Prairie Bluff Chalk contains the calcareous nannofossil *Micula prinsii*, the marker for latest Maastrichtian UC20d^{TP} subzone (e.g., Larina et al., 2016), and the ammonite *Discoscaphites iris*, indicative of the upper Maastrichtian *D. iris* Range Zone (Landman et al., 2004; Witts et al., 2021). Chemostratigraphic analysis of the chalk-marl "couplets" at Starkville suggests they are associated with precession cycles with a duration of ∼20.6 kyrs (Naujokaitytė et al., 2021), and that ∼80 kyrs of the latest Maastrichtian are missing from this locality. Our 2 m sampling interval encompasses a time interval from ∼300 to 80 kyrs prior to the K-Pg boundary.

The Prairie Bluff Chalk at TCC also contains *D. iris* along with typical uppermost Maastrichtian planktic foraminifera such as *Psuedoguembelina hariaensis* and *Pseudotextularia elegans*. The foraminiferal zonal marker for the latest Maastrichtian (*Plummerita hantkeninoides*) is absent. While this may indicate missing time due to impact-related erosion, it is also attributable to the fact that open-ocean taxa like *P. hantkeninoides* were rare in shelf depth waters like those along the Gulf Coastal Plain (e.g., Olsson et al., 1996).

For the Clayton Formation, samples within the K-Pg channel deposits, the spherule bed, and basal 30 cm of the burrowed unit contain only Cretaceous foraminifera, including many reworked taxa as well as species known to survive the extinction event. This interval is assigned to planktic foraminiferal Zone P0, defined as the interval between the top of the Cretaceous (defined as the base of the impact deposit; e.g., Molina et al., 2005) and the lowest occurrence of *Parvularugoglobigerina eugubina*. The spherule-rich beds probably represent extremely rapid deposition and reworking, on the order of months to years, like other Gulf Coast K-Pg successions (Artemieva & Morgan, 2009). The lowest occurrence of *P. eugubina* is observed 30 cm above the base of the burrowed unit, marking the boundary between Zone P0 and Zone Pα, representing ∼30 kyrs after impact based on ages from Wade et al. (2011) and Speijer et al. (2020). The disappearance of *P. eugubina* 1.1 m above the base of the burrowed unit marks the base of subzone P1a 300 kyrs after impact (Wade et al., 2011). The most common macrofossil in the burrowed unit is the oyster *Pycnodonte pulaskensis*, which occurs throughout, alongside the bivalve *Cucullaea macrodonta*. Both are considered index macrofossils for the lower Danian in the region (e.g., Toulmin, 1977).

It should be noted that although we attempted to sample away from obvious burrows, the extensive bioturbation in the burrowed unit (unit c) may mean that foraminiferal markers are reworked or blurred stratigraphically downsection. If this is the case, then the age model based on foraminiferal age constraints represents the maximum depositional age, and the unit may in fact have been deposited over much shorter timescales with concomitant effects for our MAR calculations. We use the foraminifera-based age model herein, while acknowledging that further, more detailed sedimentological study of this interval is required.

At *AMNH 3525* and away from the channel deposits at *AMNH 3944b*, the basal 10–25 cm of the Clayton Formation above the burrowed unconformity contains early Danian planktic foraminifera, and the absence of *P. eugubina* in this interval suggests correlation to subzone P1a. Successive samples, spaced every 0.5 m, in the Clayton Formation contain the first occurrences of *Subbotina triloculinoides* (0.5 m above the base), *Eoglobigerina spiralis* (1 m above the base) and *Praemurica inconstans* (∼1.5 m above the base) indicating the presence of subzone P1b followed by P1c, the bases of which are 800 kyrs and ∼2.1 myrs after the impact event, respectively. Our full composite section thus encompasses a time interval from ∼300 kyrs prior to >2.1 myrs after the K-Pg boundary.

To summarize our age model based on biostratigraphy: (a) from −2.70 m to the K-Pg boundary (Uppermost Cretaceous-Prairie Bluff Chalk) the sedimentation rate is 2.8 cm/kyrs; (b) the first 0.35 m of Paleogene, related to the ejecta layer (K-Pg boundary), represent extremely rapid deposition, potentially on the order of days to months (Artemieva & Morgan, 2009); (c) the first 0.30 m above the ejecta layer, the sedimentation rate is 1.0 cm/kyr (P0 zone); (d) from 0.30 to 1.10 m above ejecta layer, the sedimentation rate is 0.3 cm/kyrs (Pα foram zone); (e) from 1.10 to 1.60 m above ejecta layer the sedimentation rate is 0.1 cm/kyrs (P1a zone) and finally, (f) from 1.60 to 2.10 m above ejecta layer the sedimentation rate is 0.04 cm/kyrs (P1b zone) (Figure 4).

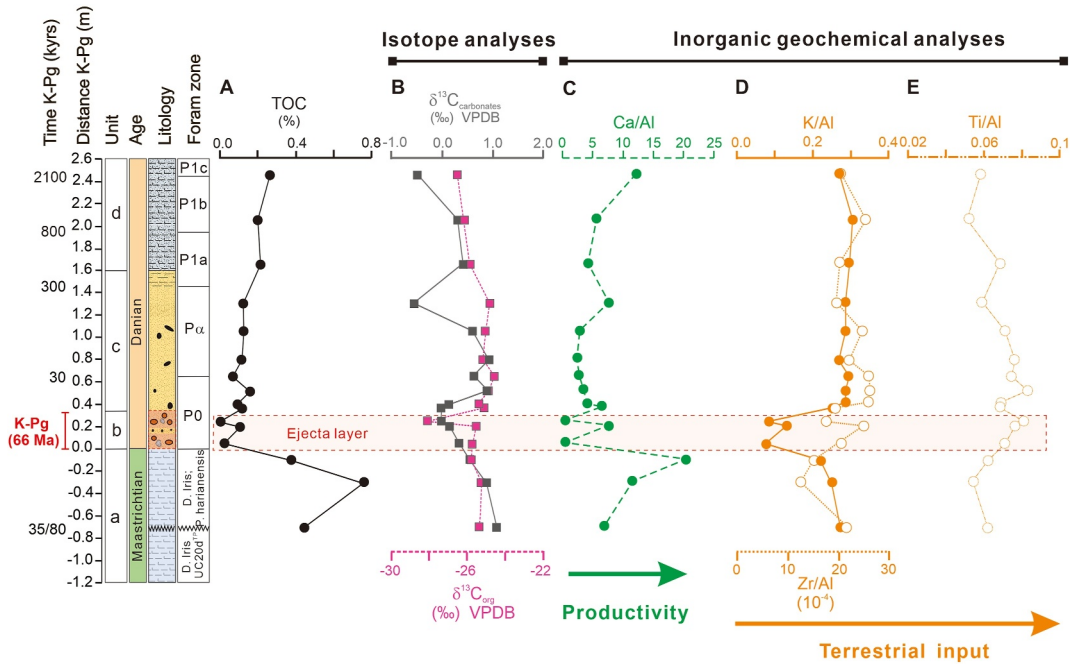

Figure 5. (a) Total organic carbon (%) from our composite K-Pg boundary profile (continuous black line). (b) Stable carbon isotope profiles (‰ V-PDB), $\delta_{13}C_{carb}$ is represented by continuous gray line and $\delta_{13}C_{org}$ by dashed pick line. (c) Ca/Al ratio (dashed green line). (d) K/Al (continuous orange line) and Zr/Al ($*10^{-4}$; dashed orange line). (e) Ti/Al ratio (discontinuous-dashed orange line). These analyses were made only in samples from the Trim Cane Creek outcrop (localities *AMNH 3944a* and *AMNH 39244b*). For lithology, see caption in Figure 3 and for data see Table S1 in Supporting Information S1.

4.2. Total organic carbon (TOC) Contents, Organic and Carbonate Carbon Isotopic Compositions, and Inorganic Geochemistry

TOC contents are less than 1% throughout the section. Maximum values were observed in the upper Cretaceous sediments (unit a), which range from c. 0.38%–0.76% (Figure 5a and Table S1 in Supporting Information S1). TOC contents are lowest in the ejecta layer (unit b), from c. 0.01%–0.12%, increase very slightly in the burrowed unit (unit c), from c. 0.08%–0.16%, and then increase slightly more in the Clayton Fm. (unit d), from c. 0.21% to c. 0.27%.

Bulk sediment $\delta^{13}C_{carb}$ ranges from c. 0.57‰–1.08‰ through unit a. It reaches minimum values, between 0.00‰ and 0.35‰, in the ejecta layer and samples from the base of the burrowed unit (units b and c, between 0.00 and 0.40 m above K-Pg). Similar values to those from the Upper Cretaceous are observed from 0.40 to 2.50 m (burrowed unit and Clayton Formation; units c and d), except for 2 samples at 1.25 m with c.—0.54‰ and at 2.50 with c.—0.47‰ (Figure 5b and Table S1 in Supporting Information S1). Bulk sediment $\delta^{13}C_{org}$ ranges from c. −25.3‰ to −25.7‰ through unit a. $\delta^{13}C_{org}$ has a minimum in the ejecta layer, between −25.5‰ and −28.0‰, before increasing again in the burrowed unit (unit c) to between −25.2‰ and −24.6‰. Similar values to those of the Upper Cretaceous are observed in the Clayton Formation (unit d), with c.—26.5‰ and at −25.8‰ (Figure 5b and Table S1 in Supporting Information S1).

Inorganic geochemical data analyzed by ICP-OES and ICP-MS (ICP-OES/MS) are presented as elemental ratios (Ca/Al, K/Al, Ti/Al and Zr/Al) across the K-Pg (Figures 3 and 5c-5e and Table S1 in Supporting Information S1). Selected Al-normalized ratios provide information about environmental variations along the ∼3.20 m-thick studied interval. Elemental ratios related to marine productivity such as Ca/Al ratios and $CaCO_3$ content decrease within the ejecta layer, with values of 4.1 for the Ca/Al ratio, and 10.26% for the $CaCO_3$ content (see Figures 3a and 5c). Typical detrital input ratios, such as K/Al, Ti/Al, and Zr/Al (Figures 5d and 5e), increase in the ejecta layer and burrowed unit (units b and c). Similar values occur in the Cretaceous (unit a) and upper Clayton unit (unit d).

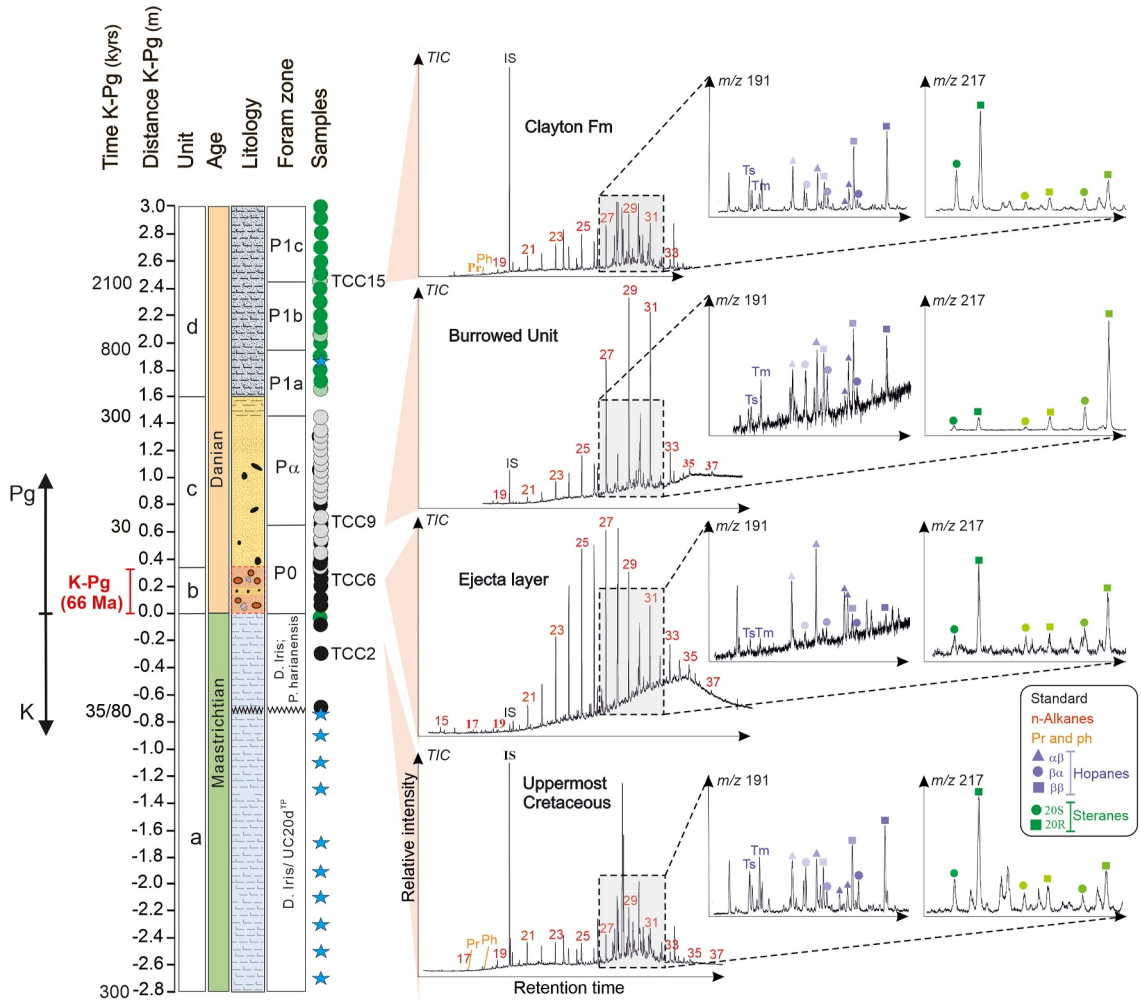

Figure 6. Apolar fractions from units a to d from Trim Cane Creek (*AMNH 3944a* black and gray colors and *AMNH 3944b* green colors) and Starkville (SA; *AMNH 3525* blue colors) K-Pg boundary sections. Total ion current chromatogram showing predominantly *n*-alkanes (red colors), Pr = pristane and Ph = phytane (orange color). Numbers correspond to carbon chain length. IS = internal standard (5α-androstane). Hopanes shown by the *m/z* 191 mass chromatogram (purple colors. C_{29}-light purple; C_{30}-intermediate purple; C_{31}-dark purple). Steranes shown by the *m/z* 217 mass chromatogram (yellow-green colors. C_{27}-light yellow; C_{28}-intermediate green; C_{29}-dark green). For lithological details see caption in Figure 3. K-Cretaceous, Pg-Paleogene.

4.3. Biomarkers

Despite relatively low TOC contents (Figure 5a), the sediments from TCC (*AMNH 3944a and AMNH 3944b*) and SA (*AMNH 3525*) K-Pg boundary sections contain a full complement of hydrocarbons (Figure 6) and polar compounds (Figure 7) from both terrestrial and marine sources (e.g., *n*-alkanes, acyclic isoprenoids, steranes, hopanes, GDGTs).

The apolar compounds' distributions and concentrations vary stratigraphically through the section (Figure 6). These sediments contain a homologous series of *n*-alkanes (Figure 6, red color) with a relatively strong odd-over-even predominance, indicating a significant terrigenous input of OM to the sediments (Cranwell et al., 1987; G. Eglinton & Clavin, 1967; G. Eglinton & Hamilton, 1967; Kvenvolden, 1967; Rieley et al., 1991). LMW *n*-alkanes ($\leq C_{21}$), typically attributed to marine sources (Cranwell et al., 1987; Schneider et al., 1970), dominate throughout unit a and d, whereas HMW homologs ($\geq C_{25}$) associated with terrestrial OM source dominate in unit b and c. Pristane and phytane (Figure 6, orange color) occur in concentrations similar to those of co-occurring LMW *n*-alkanes and they are absent in unit c. The apolar fractions also contain a series of bacterially derived C_{27} to C_{31} hopanes (Figure 6, purple color), and the eukaryote derived C_{27}–C_{29} regular steranes (Figure 6, green color),

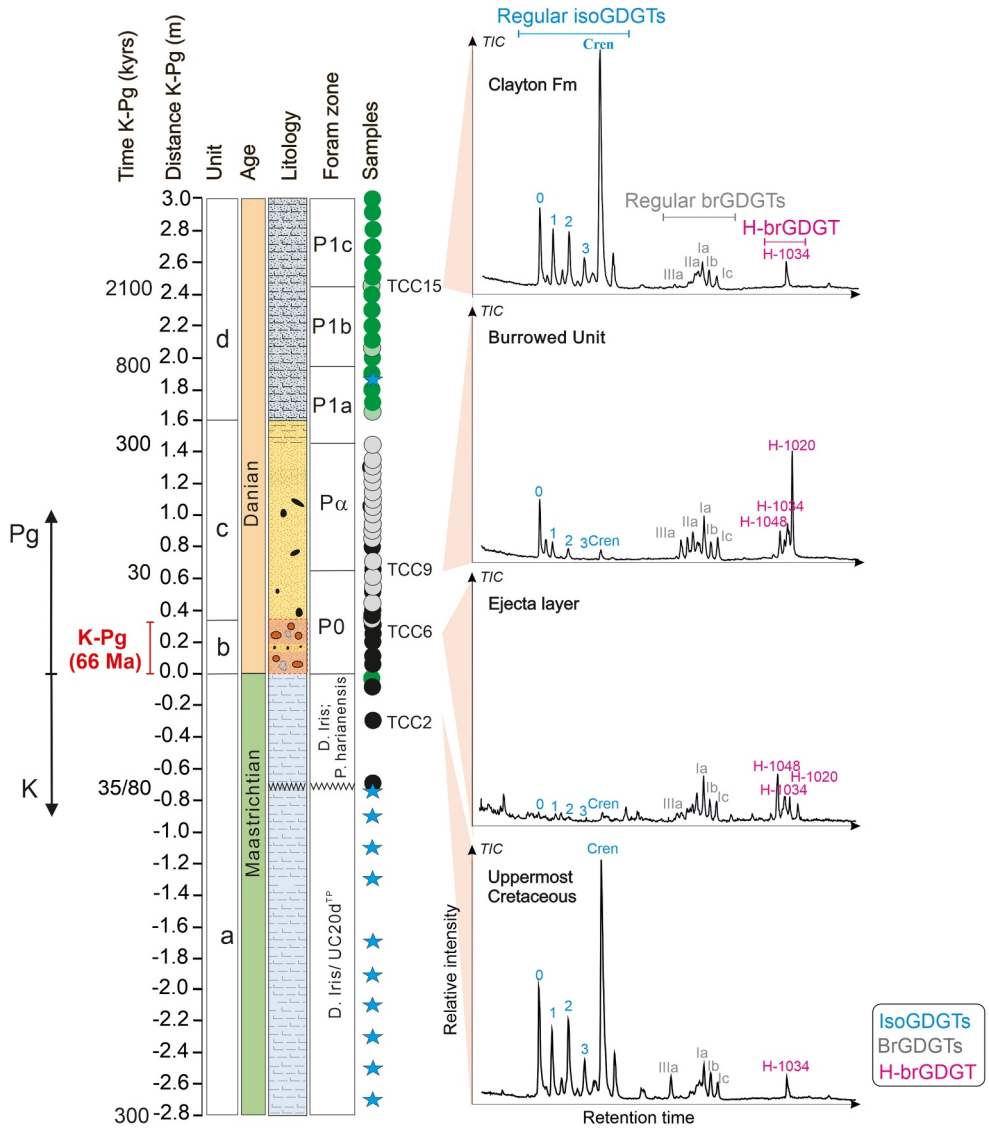

Figure 7. Polar fractions from units a to d from Trim Cane Creek (*AMNH 3944a* black and gray colors and *AMNH 3944b* green colors) and Starkville (SA; *AMNH 3525* blue colors) K-Pg boundary sections. Total ion current chromatogram showing both regular isoGDGTs (blue colors) and brGDGTs (gray color) and as well as, H-brGDGTs (pink color). For lithological details see caption in Figure 3. K-Cretaceous, Pg-Paleogene.

tetracyclic triterpanes arising from diagenetic alteration of sterols (which were also observed in the polar fractions) (e.g., Peters et al., 2005; Schwark & Empt, 2006 and references therein).

The distributions and concentration of isoprenoidal GDGTs (isoGDGTs) and branched GDGTs (brGDGTs) also vary across the K-Pg boundary (Figure 7). Intriguingly, we also detect abundant branched glycerol monoalkyl glycerol tetraethers (brGMGTs or "H-GDGTs"), which have previously been reported for ancient lignites (Naafs et al., 2018). The isoGDGTs dominate in unit a and exhibit a distribution consistent with a marine origin. All GDGT concentrations are lower in units b and c, but brGDGTs and brGMGTs are relatively more abundant, especially in the ejecta layer, indicating proportionally more significant inputs from soils and perhaps reworked lignites or peat. In unit d, distributions are similar to those in unit a.

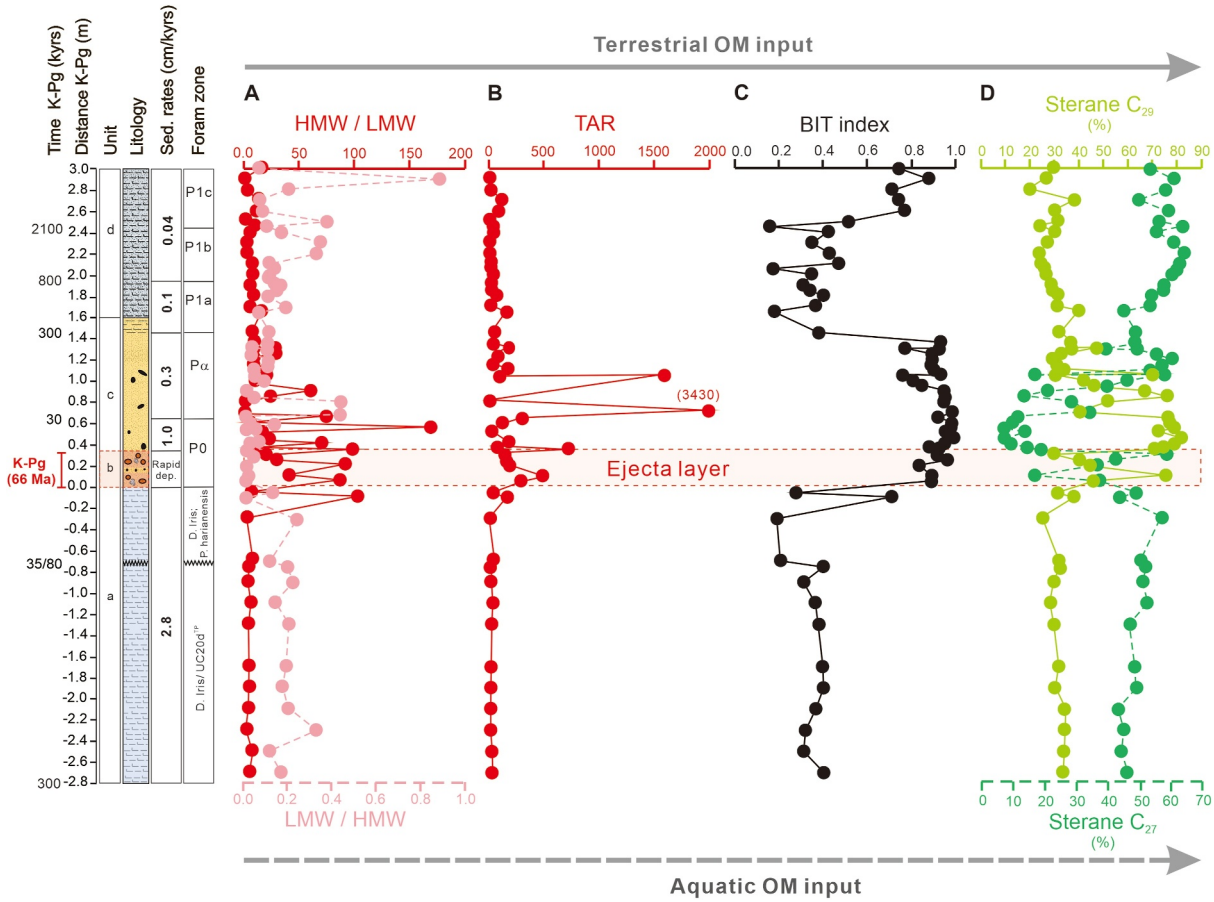

Figure 8. Concentrations and ratios of terrestrial and marine biomarkers through the composite K-Pg section. (a) HMW/LMW ratios of *n*-alkanes (continuous red line) and LMW/HMW ratios of *n*-alkanes (discontinuous light pink line) (b) terrigenous/aquatic ratios (Cranwell et al., 1987; Bourbonniere & Meyers, 1996) of *n*-alkanes $[C_{27} + C_{39} + C_{31}]/[C_{15} + C_{17} + C_{19}]$ (continuous red line). (c) BIT index (BIT = [bGDGT-I + bGDGT-II + bGDGT-III)/(bGDGT-I + bGDGT-II + bGDGT-III + crenarchaeol]) (continuous black line). (d) % of C_{29} regular sterane $[C_{29}/\Sigma(C_{27} + C_{28} + C_{29})]$ (continuous dark green color) and % of C_{27} regular sterane $[C_{27}/\Sigma(C_{27} + C_{28} + C_{29})]$ (discontinuous yellow color). The black arrow shows higher terrestrial organic matter (OM) input for upper axis parameters, and the discontinuous gray arrow shows higher marine OM input for the lower axis parameters. For lithology details, see caption in Figure 3 and see data in Table S2 in Supporting Information S1.

4.3.1. Depth Profiles of Terrestrial Biomarkers

Many of the biomarkers present and biomarker ratios calculated are related to the proportional contribution of terrestrial OM to total OM. These include high abundances of long-chain *n*-alkanes with a strong odd-over-even predominance, reflected in HMW/LMW ratios (Cranwell et al., 1987; G. Eglinton & Hamilton, 1967), terrestrial to aquatic ratios (TAR) (Bourbonniere & Meyers, 1996; Cranwell et al., 1987), and high proportions (%) of C_{29} steranes (e.g., Huang & Meinschew, 1979). In our section, *n*-alkane HMW/LMW and TAR ratios are low in uppermost Cretaceous sediments (unit a) and the upper part of the Clayton Fm. (unit d), with higher values in the ejecta layer (unit b) and burrowed unit (unit c) (Figures 8a and 8b and Table S2 in Supporting Information S1). C_{29} steranes are strongly dominant relative to C_{27} and C_{28} components in units b and c but have lower proportions in unit d (Figure 8d). A terrestrial source is also supported by the presence of branched GDGTs (brGDGTs) which are inferred to represent fluvially transported soil OM (Schouten et al., 2013) (Figure 7). The Branched Isoprenoid Tetraether (BIT; Hopmans et al., 2004) index is a proxy for the input of soil terrestrial OM into aquatic environments, and typical values in terrestrial soils and marginal marine sediments are >0.9, whereas in open marine settings they are usually below 0.6 (Weijers et al., 2006). In our profile, the BIT index is relatively low (<0.4; see Figure 8c) for the Cretaceous and for the Clayton Fm. (units a and d), but increases sharply in the ejecta layer (unit b) and burrowed unit (unit c) (~1.0; see Figure 8c), indicating a significant soil OM input relative to marine OM in

these units (Table S2 in Supporting Information S1). BIT indices are also high in the uppermost 30 cm of the Clayton Fm (~0.8; see Figure 8c).

4.3.2. Depth Profiles of Marine Biomarkers

Evidence for marine OM input is suggested by the abundant LMW alkanes, pristane and phytane. The LMW/HMW ratio (Ali & Mudge, 2006; Carrie et al., 1998) is highest in uppermost Cretaceous sediments (unit a), then decreases very rapidly in the ejecta layer (unit b) and burrowed unit (unit c), before increasing again in the upper part of the Clayton Fm. (unit d) (Figure 8a and Table S2 in Supporting Information S1). The putative algal chlorophyll degradation products, pristane and phytane (Dean & Whitehead, 1961; Rontani & Volkman, 2003), are present in the upper Cretaceous sediments but undetected in the bottom part of the burrowed unit. They re-occur in the Clayton Formation (unit d), albeit at lower abundances than in the Cretaceous (Figure 6). C_{27} sterane proportions (%) are high (e.g., Huang & Meinschew, 1979) in units a and d and lower in units b and c (Figure 8d). Similarly, the presence of crenarchaeol and low BIT indices indicate strong marine archeal inputs in units a and d (Figures 7 and 8c).

4.4. Relative Mass Accumulation Rates

LMW *n*-alkanes, hopanes, C_{27} sterane, pristane, phytane and GDGTs, especially isoGDGTs, all exhibit highest relative MARs in sediments from the Upper Cretaceous (unit a) (Figures 9a–9e). MARs for the same biomarkers are 3 to 4× lower (or more) in Paleogene sediments (units b-c), except for pristane and phytane which exhibit even more extreme differences, being either absent in the burrowed unit c or having relative MARs up to 30× lower than in the Cretaceous sediments. Relative MARs of putative aquatic biomarkers remain low in unit d, even though biomarker assemblages resemble those of the Cretaceous sediments. Relative MARs of terrestrial biomarkers, including HMW *n*-alkanes and the C_{29} sterane, exhibit opposite trends, being very high at the base of the burrowed unit and significantly lower in the Upper Cretaceous (unit a) (Figures 9a and 9c). In the case of the ejecta layer (unit b), we did not calculate MAR because this layer was deposited rapidly, potentially on the order of days to months (Artemieva & Morgan, 2009) (Figure 9); if done, such calculations would yield markedly high MARs for terrestrial biomarkers.

4.5. Changes in Apparent Thermal Maturity

The OM in our composite section appears to be thermally immature. The biologically produced and thermally unstable 17β(H),21β-homohopane ($C_{31}\beta\beta$ hopane) and 17β(H),21β hopane ($C_{30}\beta\beta$ hopane) isomers are present (Mackenzie et al., 1980; Ourisson et al., 1979; Peters & Moldowan, 1991; Seifert & Moldowan, 1980); in fact, these isomers often dominate and ratios for C_{30} and C_{31} [17β(H), 21β/(17β(H), 21β + 17α(H), 21β + 17β(H), 21α)]-hereafter $\beta\beta/(\beta\beta + \alpha\beta + \beta\alpha)$ are typically >0.60 (Figure 10 and Table S2 in Supporting Information S1). Consistent with this, functionalized compounds such as GDGTs are detected in all samples, and only the 5α, 14α,17α epimers (both 20S and 20R) of the three regular $C_{27\text{-}29}$ steranes are present.

However, important changes occur through the section. Maximum C_{30} and C_{31} $\beta\beta/(\beta\beta + \alpha\beta + \beta\alpha)$ ratios (0.6, indicating very low thermal maturity) occur in the Cretaceous (unit a) and the Clayton Fm (unit d). However, values are much lower (~0.3) in the ejecta layer (unit b), burrowed unit (unit c) and upper 60 cm of the Clayton Fm (unit d) (see Figure 10 and Table S2 in Supporting Information S1). Given the thickness of this section, variation in thermal history is not expected, and thus we assume this is related to a change in OM source, such as the erosive delivery of older reworked petrogenic OM (i.e., Handley et al., 2010) (see discussion below).

5. Discussion

In previous biomarker work focused on several distal K-Pg sites, such as the Stevns Klint, Denmark and the Mid-Waipara, New Zealand neritic sections (Bralower et al., 2020; Sepúlveda et al., 2009; Sosa-Montes de Oca et al., 2021, 2023) and the Agost, Spain bathyal section (Sosa-Montes de Oca et al., 2021), only relatively minor changes were observed in the biomarker assemblages, and by inference, in the non-fossilizing phytoplankton community across the boundary. Moreover, even these modest changes were followed by a rapid recovery to pre-K-Pg assemblages. However, here we observe dramatic changes. We first interpret biomarker assemblages to explore changes in the OM source in the composite proximal K-Pg boundary section (from two outcrops; TCC [localities *AMNH 3944a* and *AMNH 3944b*] and SA [locality *3525*]). Then, we focus on two aspects of

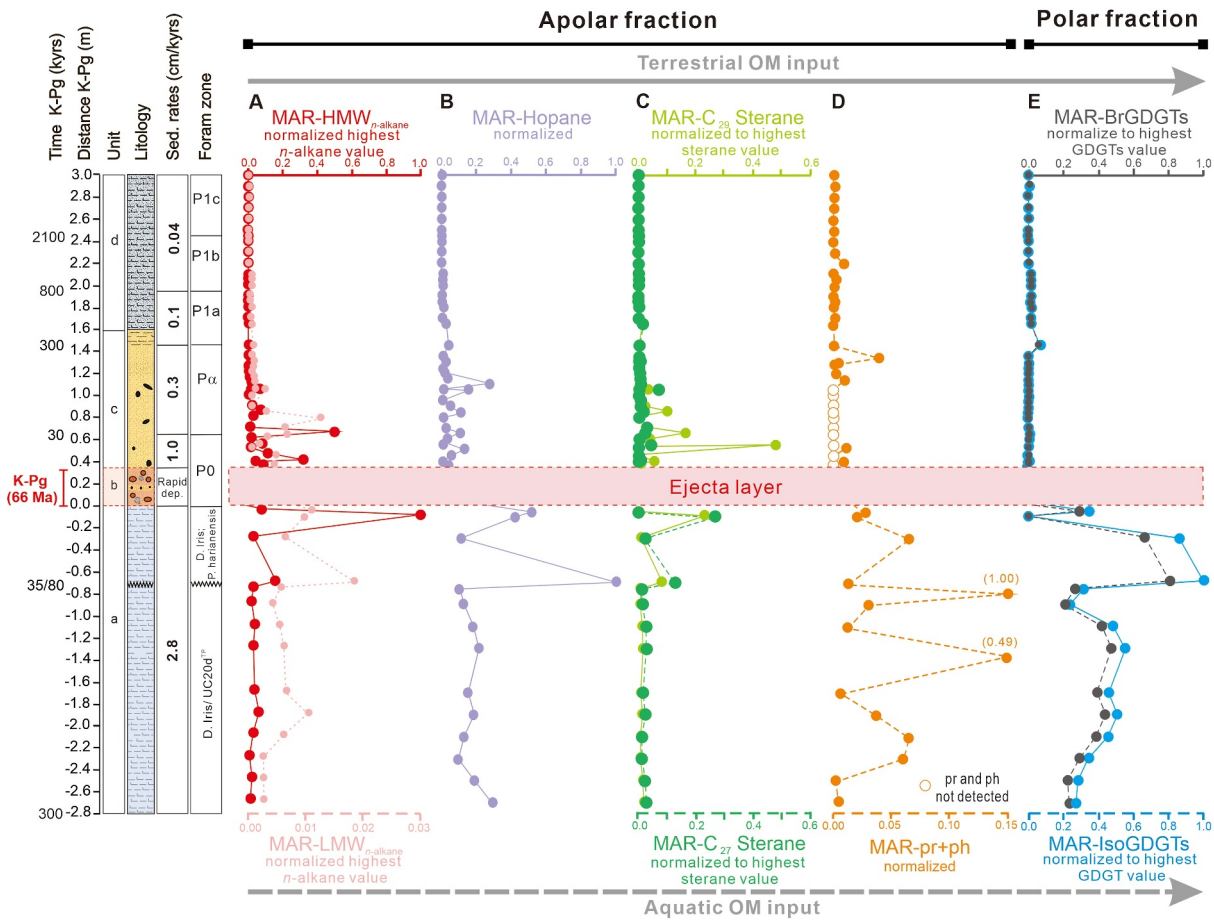

Figure 9. Relative mass accumulation rates (normalized to sample with highest abundance) of apolar and polar biomarkers across the K-Pg boundary in our composite section: (a) *n*-alkanes (LMW—dashed light red and HMW—continuous red). (b) mass accumulation rate (MAR) hopanes (continuous purple line). (c) Steranes (C_{27}—dashed green line and C_{29}—continuous light green line). (d) Pristane (Pr) plus phytane (Ph) (discontinuous orange line); glycerol dialkyl glycerol tetraether lipids (GDGTs) (isoGDGTs in blue and brGDGTs in gray). We did not calculate MAR in the ejecta layer. The black arrow shows higher terrestrial organic matter (OM) input for upper axis parameters, and the discontinuous gray arrow shows higher marine OM input for the lower axis parameters. For lithology details, see caption in Figure 3 and Table S3 in Supporting Information S1.

environmental, biotic and OM source change: (a) the sedimentological change and associated rapid and dramatic increase in terrestrial OM in post-K-Pg sediments; and (b) the rapid decline in algal biomarker proportions and MARs and coinciding decline in $CaCO_3$ MARs at the K-Pg boundary and the slow apparent recovery.

Significant changes occur in biomarkers ratios (Figures 8 and 10) and relative MARs (Figure 9) through our composite section. These are related primarily to changes in the marine (or aquatic) versus terrestrial sources of OM across the K-Pg boundary and during the early Paleogene. Overall, biomarkers indicate a mixed source assemblage between terrestrial, marine, and reworked petrogenic OM, but their relative proportions change dramatically through the different units.

The uppermost Cretaceous sediments (unit a) are dominated by a typical marine OM assemblage, reflected by high LMW/HMW *n*-alkane ratios (Figures 8a and 8b), high C_{27} sterane percentages (Figure 8d), highest pristane and phytane relative MARs (Figure 9d), and low BIT indices (Figure 7). Furthermore, abundant crenarcheaol and high GDGT-2/GDGT-3 ratios could also indicate an active biological pump (Taylor et al., 2018). All of these data indicate a dominance of marine OM inputs, as expected from a neritic marine environment, and suggest a vibrant and diverse algal ecosystem prior to the meteorite impact event and related mass extinction.

Within the ejecta layer (unit b), which represents an instantaneous deposit (Artemieva & Morgan, 2009), LMW/HMW *n*-alkane ratios and C_{27} sterane proportions are lower, and pristane + phytane relative MARs are very low. At the same time, BIT indices, HMW/LMW and TAR *n*-alkane ratios and C_{29} sterane percentages all increase

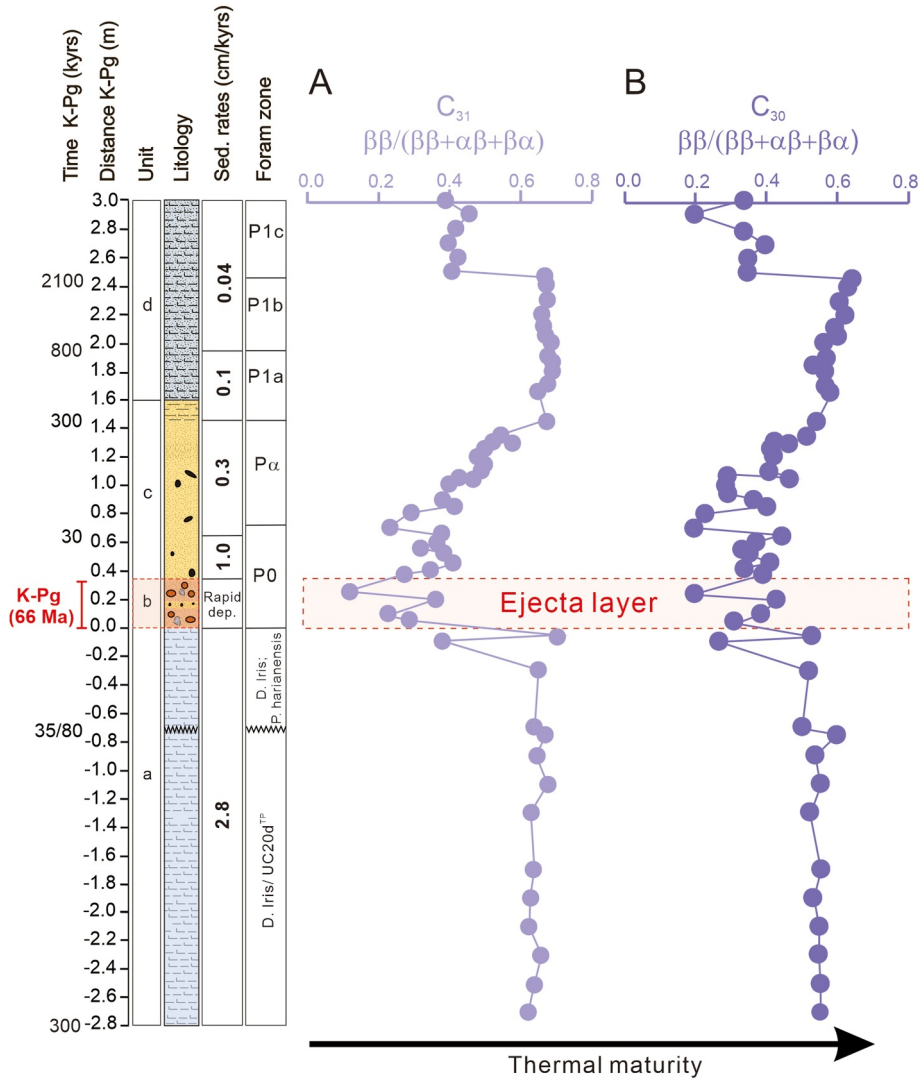

Figure 10. Biomarker ratios indicative of the thermal maturity at our composite profile from K-Pg boundary. (a) *ββ*/(*ββ* + *αβ* + *βα*) C_{31} hopane ratio (continuous light purple line). (b) *ββ*/(*ββ* + *αβ* + *βα*) C_{30} hopane ratio (continuous dark purple line). Black arrows show higher thermal maturity. For lithology details see caption in Figure 3 and for data see Table S2 in Supporting Information S1.

dramatically (Figures 8a–8d), indicating a dramatic change to predominantly terrestrial OM sources. It is somewhat enigmatic how soil OM has been incorporated into the geologically instantaneous ejecta layer deposit; this could either indicate rapid mobilization of terrestrial matter in the immediate aftermath of the impact or post-depositional reworking.

Within the burrowed unit (unit c), which represents the first 450 kyr post-KPg, biomarker assemblages are initially similar to those of the ejecta layer. In the first 0.70 m of this unit c, ∼160 kyrs after the impact event, LMW *n*-alkane and C_{27} sterane relative MARs (Figures 9a and 9c) and LMW/HMW ratios (Figure 8a) are low; moreover, pristane and phytane (Figure 9d) (Dean & Whitehead, 1961; Rontani & Volkman, 2003) and crenarchaeol (Figure 7) could not be detected. Concurrently, high BIT indices (Figure 8c) and high HMW *n*-alkane and C_{29} sterane MARs indicate strong terrestrial inputs (Figures 9a and 9c). In the next 0.30 m of unit c, the concentrations of pristane + phytane and LMW *n*-alkanes increase. C_{29} sterane relative MARs and proportions remain high but begin to decrease (Figure 9c), as do BIT indices and HMW/LMW *n*-alkane ratios, all suggesting lower terrigenous OM inputs (Figure 8c). In the last 0.15 m of the burrowed unit and in the lower part of the Clayton Fm. (unit d), from ∼280 kyrs to ∼3 Myrs, all biomarker ratios seem to have similar values to the

uppermost Cretaceous. However, relative MARs remain very low for LMW *n*-alkanes, C_{27} sterane and pristane and phytane (Figures 9a–9d) compared to those from the uppermost Cretaceous. This arises not from lower biomarker concentrations but lower sedimentation rates. Therefore, these low MARs also indicate that calcareous primary producer export productivity also did not return to late Cretaceous values during the entirety of our study time interval.

In summary, all of our biomarker indices and relative MARs are consistent, indicating a dramatic increase in terrestrial OM and decrease in algal/aquatic OM in the immediate aftermath of the K-Pg event for both the ejecta layer and burrowed unit. These likely indicate an erosive sedimentary regime coincident with the immediate aftermath of the Chicxulub impact (Section 5.1), a near-total collapse of the marine phytoplankton community (Section 5.2) or a combination of both scenarios.

5.1. Intense Erosion Directly Following the K-Pg Impact Event

The increased erosion/transport of terrestrial OM to the ocean during the first 280 kyrs after the Chicxulub impact event represents not just plant OM inputs but also soil inputs as documented by high BIT indices. Previous work has documented similar increases in terrestrial OM inputs directly following the K-Pg impact (Sosa-Montes de Oca et al., 2021, 2023), including a dramatic increase in BIT indices from the nearby open marine, mid-shelf Brazos-1 outcrop (Texas, USA) (Vellekoop et al., 2018). Intriguingly, thermal maturity indices likely indicate the co-occurring delivery of reworked kerogen. Hopane thermal maturity parameters increase dramatically in the ejecta layer and exhibit profiles remarkably similar to those of biomarker indices for terrestrial inputs. Given the thickness of the section, this cannot represent a true thermal maturity signal and instead must represent the delivery of reworked thermally mature OM, as has been inferred for the PETM (Handley et al., 2011; Hollingsworth et al., 2024; Lyons et al., 2019). Thus, the elevated plant and soil biomarker inputs in units b and c likely represent a rapid change in the depositional environmental at the K-Pg, which can be attributed to a change in erosional and deposition conditions, for example, a change to a more erosive sedimentary regime.

Previous biomarker analyses have detected a similar, albeit less dramatic, input of older reworked OM in some K-Pg distal sections, such as the Agost and Caravaca sections (Spain) (Mizukami et al., 2014; Sepúlveda et al., 2019; Sosa-Montes de Oca et al., 2021; Vellekoop et al., 2018) the Mid-Waipara river section (New Zealand) (Sosa-Montes de Oca et al., 2023) and Stevns Klint (Denmark) (Vellekoop et al., 2018). We suggest that this sedimentary terrestrial input in the post-K-Pg interval is more evident in proximal sites due to a more intense modification of land cover in North America caused by the blast wave, tsunami, and widespread forest fires that would have facilitated more intense erosion (Lyons et al., 2020), and consequently, contributed to the expanded nature of the lower Paleogene succession (the ejecta layer and potentially the basal part of the burrowed unit).

In addition, an unexpected positive carbon isotope excursion (+CIEs) occurs in both the $\delta^{13}C_{carb}$ and $\delta^{13}C_{org}$ records (Figure 5) during both the ejecta layer and lower part of the burrowed unit (P0 and Pα). This was also observed in the $\delta^{13}C_{org}$ record of the distal Agost section (Spain) (Sepúlveda et al., 2019; Sosa-Montes de Oca et al., 2021) and in the Mid Waipara section (New Zealand) (Sosa-Montes de Oca et al., 2023). Generally, a negative carbon isotope excursion (-CIE), in both $\delta^{13}C_{carb}$ and $\delta^{13}C_{org}$, is expected at the post-K-Pg boundary (H. S. Birch et al., 2016; Sepúlveda et al., 2019) as a result of the release and/or inefficient burial of ^{13}C-depleted carbon. Consequently, the +CIE in our record could be related to a transient pulse of reworked ^{13}C-enriched kerogen, also in agreement with the changes observed in the C_{30} and C_{31} hopane ratios (Figure 10). Although it is unclear what the specific source of ^{13}C-enriched OM would have been, the impact of reworked OM on the fidelity of the bulk organic carbon isotopic record has been documented previously (Carmichael et al., 2019). This increase of terrestrial OM is also supported by higher values in detrital input ratios like, K/Al, Ti/Al, and Zr/Al (Figure 5) in both the ejecta layer and lower part of the burrowed unit.

The intensification of terrestrial organic and detrital inputs appears to have been initiated nearly immediately at the K-Pg and then persisted for longer-term timescales (~160–280 kyr depending on parameter and age model). The former is illustrated by the presence of terrestrial biomarkers in the ejecta layer, which means that soil or plant matter could have been rapidly mixed into the ejecta sediments (excluding subsequent reworking). Such a rapid response is also consistent with a dramatic but transient increase in BIT indices associated with a storm/tsunami deposit in the mid-shelf Brazos-1 section (Vellekoop et al., 2018). A rapid influx in terrigenous material could have contributed to the thickness of the ejecta layer in this proximal section: ~0.35 m thick compared to ~0.002 m in distal K-Pg sections like Caravaca and Agost in Spain. Given its apparent rapidity, we suggest that the

enhanced terrestrial inputs could reflect the direct response to a tsunami in the Gulf region (Kinsland et al., 2021; Smit et al., 1996) or other consequences of impact-associated seismic events (DePalma et al., 2019; Sanford et al., 2016).

Based on our age model, the suppression of carbonate deposition and dominance of terrestrial OM inputs, including soil, plant and reworked kerogen biomarkers as well as lignite fragments, persisted for about 280 kyr. Detrital inputs persisted for about 160 kyr. This indicates that the change in the sedimentary regime at this site persisted for 100 s of thousands of years and that the change in biomarker and sedimentary regime was probably not the consequence of a single erosive event, for example, a tsunami deposit. The persistence of this perturbation differs from other settings, for example, the mid-shelf Brazos-1 section (Texas), where elevated BIT indices are transient and only associated with a tsunami/storm deposit (Vellekoop et al., 2018). A possible mechanism for prolonged perturbation is local suppression of primary productivity and associated low carbonate sedimentation rates (see Section 5.2), such that detrital sedimentation dominated. Olsson et al. (1996) speculated that the abrupt transition from the Prairie Bluff Chalk to the more siliciclastic Clayton Formation in the eastern Gulf Coastal Plain partly reflected the mass extinction of carbonate producers at the K-Pg with concomitant effects on sedimentation rate. Alternatively, it could reflect reorganization of the local sedimentary system along the Gulf Coast, including progradation of the shoreline driven by the massive increase in erosion or subsidence of the continental margin that occurred in the immediate aftermath of the impact. Such a temporal coincidence has also been considered plausible by Savrda (2018) based on paleontological and sedimentological data from the lithologically similar K-Pg outcrops at Moscow Landing, Alabama. Related to those mechanisms, elevated erosion and terrestrial inputs to the Gulf Coastal Plain could have persisted due to the extensive loss and slow recovery of terrestrial biomass across the North American continent (Morgan et al., 2022). Recently, Henehan et al. (2019) and Junium et al. (2022), presented evidence for deposition of large quantities of atmospheric sulfur following the Chicxulub impact in both distal and proximal K-Pg sections, and this was likely associated with intense acid rain (Kring, 2007; Morgan et al., 2022). Although sulfur residence time in the atmosphere is less than 5 years (Senel et al., 2023), the impacts of acid rain on soil quality could have inhibited biotic recovery on longer timescales.

Alternatively or additionally, this increase in the terrestrial OM could also provide evidence that sea level does lower across our studied K-Pg boundary. Our composite section could therefore represent a mixture of impact-related processes and increased input from nearer shore environments related to lowered sea level as has been proposed in other K-Pg sites (Adatte et al., 2002; Habib et al., 1992; Kominz et al., 2008; Macleod & Keller, 1991; Miller et al., 2005; Schulte et al., 2006). However, based on detailed study of Gulf Coast K-Pg successions, it is considered unlikely that local sea level in the Gulf Coastal Plain fell beyond the shelf break across the K-Pg boundary (Hart et al., 2013; Schulte & Speijer, 2009). Regardless of mechanism, it is clear that the coastal Gulf Plain experienced a rapid but also long-term reorganization of its sedimentary regime, characterized by increased detrital inputs, including reworked lignite fragments, as well as plant, soil and reworked kerogen biomarkers.

5.2. Decrease and Slow Recovery of Marine Primary Production

A post K-Pg near-collapse of marine phytoplankton export production at this location is supported by the sharp decrease of relative MARs of all marine biomarkers (LMW *n*-alkane and C_{27} sterane and IsoGDGTs; Figures 9a, 9c, and 9e) within the first centimeters of unit c, just above the ejecta layer. It is also supported by the total absence of the putative algal chlorophyll degradation products pristane and phytane (Figure 9d) (Dean & Whitehead, 1961; Rontani & Volkman, 2003), and trace crenarchaeol abundances after the K-Pg boundary (Figure 7). A collapse of marine production is consistent with the relative decrease of marine versus terrestrial OM input ratios (LMW/HMW) and the percentage of C_{27} sterane (Figures 8a and 8d), although changes in these parameters will also reflect the erosional event(s) discussed above.

The Chicxulub impact caused a global decrease in productivity in the world's oceans (Alvarez et al., 1980; Schulte et al., 2010; Smit & Hertogen, 1980). However, this has not always been evident in biomarker assemblages from distal sites (Sepúlveda et al., 2009; Sosa-Montes de Oca et al., 2021, 2023). In contrast, our data suggest a decrease in the flux of marine OM to the seafloor in the immediate aftermath of the impact and mass extinction on the Gulf Coastal Plain. The contrast with previous biomarker studies likely reflects a more pronounced impact on more proximal communities and highlights the importance of developing a global perspective on changing biomarker assemblages.

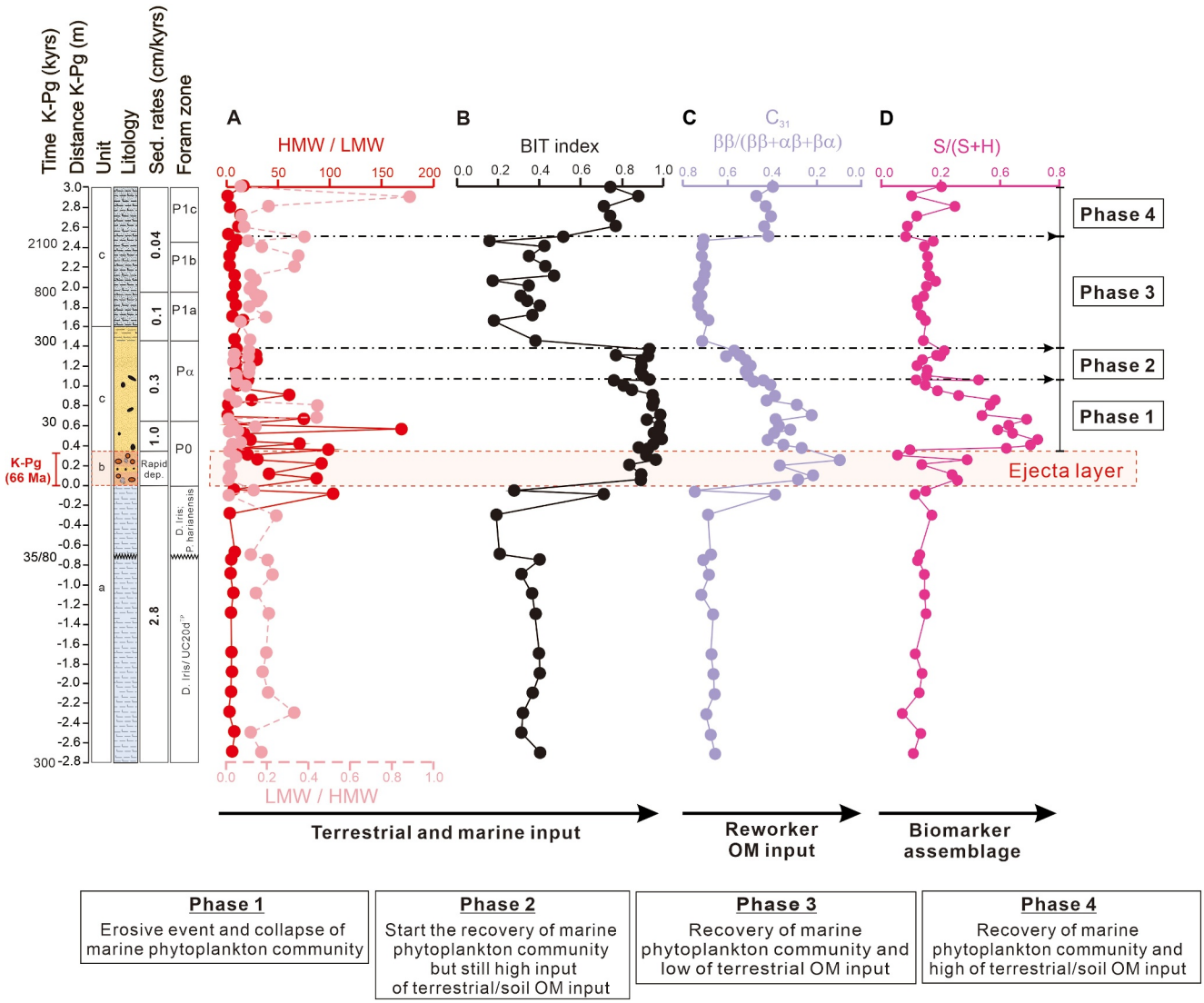

Figure 11. Main ratios and profiles across K-Pg boundary. (a) HMW/LMW ratio of *n*-alkanes (continuous red line) and LMW/HMW ratio of *n*-alkane (dashed light red line). (b) BIT index (BIT = [brGDGT-I + brGDGT-II + brGDGT-III]/[brGDGT-I + brGDGT-II + brGDGT-III + crenarchaeol]) (continuous black line). (c) $\beta\beta$/($\beta\beta + \alpha\beta + \beta\alpha$) C_{31} hopane ratio (continuous purple line) (note reversed axis). (d) Sterane/hopane ratio (S/S + H) [$\Sigma(C_{27} + C_{28} + C_{29})$/$(C_{27} + C_{28} + C_{29}) + (\Sigma C_{27}+\cdots+C_{32})$] (continuous pink line). Black arrows show higher terrestrial organic matter (OM) input (HMW/LMW, BIT index), marine OM input (LMW/HMW), reworked OM input (C_{31} hopane ratio) and biomarker assemblages (S/(S + H)). For lithology details see caption in Figure 3 and Table S2 in Supporting Information S1.

Our biomarker analyses also suggest several phases or stages (Figure 11) in the recovery of the marine OM input that parallel the apparent slow return to the late Cretaceous depositional environment discussed above (Section 4.1). The initial decrease in marine production appears to have persisted for ~160 kyrs after the impact event (Phase 1), as documented by very low LMW *n*-alkane, C_{27} sterane and isoGDGT relative MARs (Figures 9a, 9c, and 9e) and an absence of detectable pristane, phytane (Dean & Whitehead, 1961; Rontani & Volkman, 2003) and crenarchaeol (Figure 7). Between ~160 and ~280 kyrs after the K-Pg (Phase 2), the initial recovery of the primary marine phytoplankton community occurs. At that time, some biomarker distributions [S/(S + H); Figure 11d] and sterane assemblages (Figure 8d) return to pre-K-Pg boundary values. Moreover, pristane, phytane and crenarchaeol concentrations increase to detectable levels (Figures 9d and 9e) despite remaining very low compared to those of the Upper Cretaceous. Between ~280 and ~2,200 kyrs after K-Pg (Phase 3), nearly all biomarker ratios recover to pre-boundary values. However, marine biomarker relative MARs and $CaCO_3$ sedimentation rates

remain much lower than for the pre-K-Pg, suggesting that either recovery was incomplete, or the sedimentary regime remained altered.

Our results agree with some aspects of previous studies but not others, indicating a heterogenous response either geographically or among proxies that document different aspects of the marine biota. For example, decreased primary productivity is consistent with foram assemblages from the neritic/upper bathyal Mexican sections (described by Alegret et al., 2022, 2001), but not with proximal but open marine sections from the Gulf of Mexico and Caribbean (IODP Site M0077 in the Chicxulub crater, DSDP Site 95 in the Gulf of Mexico, ODP Sites 999 and 1001 in the Caribbean) which show elevated export production via Ba/Ti ratios and other proxies (Lowery & Bralower, 2022; Lowery, Leckie, et al., 2018, 2021). They remain elevated for ∼300 kyr after the boundary, followed by a longer period of decline. This local period of high export productivity occurs over the same timescale (foraminiferal zones P0 and Pα) as our phase 1 and 2, in which minimal values in marine productivity proxies are inferred. Although this could suggest a difference between coastal and open marine settings, our findings also differ from those at Brazos-1, another mid-shelf section. There, dinoflagellate assemblages indicate an increase in nutrient richness, and the authors invoke elevated export production as a cause for bottom water hypoxia (Vellekoop et al., 2018). This adds to the complex picture of regional heterogeneity in productivity in the aftermath of the Chicxulub impact (e.g., H. Birch et al., 2021; Esmeray-Senlet et al., 2015; Hull & Norris, 2011).

We argue that heterogeneity in productivity in the aftermath of the Chicxulub impact in different neritic/bathyal sites from the Gulf of Mexico is a consequence of different local responses to the post-K-Pg sedimentary and environmental regime change, as inferred from the change in lithology, sedimentation rates and biomarker assemblages, and interpreted in Section 5.1 as an interval of enhanced erosion. An erosive regime could have suppressed marine production in the marginal Gulf Coast region, especially where it has directly impacted the sedimentary system and lithology. Although increased erosion is typically associated with nutrient inputs and high productivity (Li et al., 2024), this would be complicated by high sediment loads that can induce light limitation (Gao et al., 2023). At the same time, persistent inputs of terrestrial sediments could drive shifts in nutrient cycling like those observed in open-ocean oligotrophic ecosystems (Lowery & Bralower, 2022; Lowery, Leckie, et al., 2018; Lowery et al., 2021). Consistent with this, other mid-shelf sites such as Brazos-1 that did not experience the long-term change in depositional environment and lithology appear to have experienced increased algal productivity. Such a mechanism also explains why the Gulf Coast marine biomarker assemblages exhibit different behavior from the distal sites that record more minimal and briefer perturbations (Sepúlveda et al., 2009; Sosa-Montes de Oca et al., 2021, 2023; Vellekoop et al., 2018). We note, however, that some of the different inferred productivity records are associated with the application of different proxies, such that conflicting records could document heterogeneous responses among algal groups.

Regardless of mechanism, our results indicate that the primary marine non-fossilizing phytoplankton community was seriously impacted at proximal neritic K-Pg boundary sites (located ∼1,500 km distance from the Chicxulub impact site). This is in agreement with the reorganization seen in benthic foraminifera, that is, infaunal morphogroups, that drastically decreased at the K-Pg boundary reflecting a sudden drop in the food supply to the sea-bottom floor (Alegret et al., 2002). The local recovery of the non-fossilizing phytoplankton community, in terms of MARs, starts ∼160 kyrs after impact, but there is no return to Cretaceous values within our full study interval, representing >3 myr after the K-Pg boundary. This is long after the previously suggested global recovery of export production at 1.8 myr defined by carbon isotopes (H. S. Birch et al., 2016) and highlights the disproportionately long duration of Earth System recovery in some regions following the extremely rapid environmental changes driven by the Chicxulub asteroid impact.

6. Conclusion

We analyzed a ∼6 m composite interval from a K-Pg boundary section in the Mississippi Embayment, Gulf Coastal Plain (USA), a site that is proximal to the Chicxulub impact site. We used biomarkers, sedimentology and inorganic geochemical parameters to ascertain the changes in local environmental conditions after this mass extinction event and the response of non-fossilizing phytoplankton. We compare changes in OM sources using a range of apolar (*n*-alkanes, acyclic isoprenoids, steranes and hopanes) and polar (BIT index) biomarkers. These show intense changes in the OM sources in the immediate aftermath of the K-Pg boundary, indicating a collapse of the marine non-fossilized phytoplankton community coinciding with a long-term erosive regime that transferred terrestrial organic carbon to the ocean. Aspects of these changes persisted for as much as 280 kyrs after the

impact event, indicating a locally long-term sedimentary, environmental and ecological disruption. The local recovery of the non-fossilizing phytoplankton community, in terms of biomarker MARs, starts ∼160 kyrs after impact, but there is no return to Cretaceous values within our full study interval, representing >3 myr after the K-Pg boundary. These regional data suggest a fundamental disconnect between the recovery of export productivity on the shelf and in the open ocean in the Gulf of Mexico/Caribbean, which may be due to a long-term change in the local sedimentary system in neritic settings or variations in ecosystem functions among those different environments.

Data Availability Statement

The processed data used in this study are available at OSF and associated with a CC-By Attribution 4.0 International license (Sosa-Montes de Oca, 2024).

Acknowledgments

The authors wish to thank the NERC (contract no. NE/V003917/1) and funding from the European Research Council under the European Union's Seventh Framework Programme (FP/2007–2013) and European Research Council Grant Agreement number 340923 for funding GC-MS capabilities. C.S.M.O. acknowledges to Newton International post-doctoral fellowship from Royal Society (project reference NIF\R1\191430) and Marie Curie individual fellowship from the European Commission (project reference 101022128-EPROAMA). R.D.P. acknowledges funding from UKRI for the Frontiers Research Grant "Climate, Carbon and Energy in ancient Earth Systems" (CERES). C.M.L. and L.E.K. acknowledge NSF-OCE-2037752. C.E.M. and N.H.L. acknowledge support from NSF Grant 1924807. We thank George Phillips (Mississippi Museum of Natural Sciences) for facilitating access to the outcrops, and to the landowner at Trim Cane Creek for allowing access to private land for sampling.

References

Adatte, T., Keller, G., & Stinnesbeck, W. (2002). Late Cretaceous to early Paleocene climate and sea-level fluctuations: The Tunisian record. *Palaeogeography, Palaeoclimatology, Palaeoecology*, *178*(3–4), 165–196. https://doi.org/10.1016/s0031-0182(01)00395-9

Alegret, L., Arenillas, I., Arz, J. A., Liesa, C., Meléndez, A., Molina, E., et al. (2002). The Cretaceous/tertiary boundary: Sedimentology and micropalaeontology at El Mulato section, NE Mexico. *Terra Nova*, *14*(5), 330–336. https://doi.org/10.1046/j.1365-3121.2002.00425.x

Alegret, L., Arreguín-Rodríguez, G. J., & Thomas, E. (2022). Oceanic productivity after the Cretaceous/Paleogene impact: Where do we stand? The view from the deep. In *Special paper of the geological Society of America* (pp. 449–470). Geological Society of America. https://doi.org/10.1130/2022.2557(21)

Alegret, L., Molina, E., & Thomas, E. (2001). Benthic foraminifera at the Cretaceous-Tertiary boundary around the Gulf of Mexico. *Geology*, *29*(10), 891–894. https://doi.org/10.1130/0091-7613(2001)029<0891:bfatct>2.0.co;2

Alegret, L., & Thomas, E. (2005). Cretaceous/Paleogene boundary bathyal paleo-environments in the central North Pacific (DSDP Site 465), the Northwestern Atlantic (ODP Site 1049), the Gulf of Mexico and the Tethys: The benthic foraminiferal record. *Palaeogeography, Palaeoclimatology, Palaeoecology*, *224*(1–3), 53–82. https://doi.org/10.1016/j.palaeo.2005.03.031

Alegret, L., Thomas, E., & Lohmann, K. C. (2012). End-Cretaceous marine mass extinction not caused by productivity collapse. *Proceedings of the National Academy of Sciences of the United States of America*, *109*(3), 728–732. https://doi.org/10.1073/pnas.1110601109

Ali, M. M., & Mudge, S. M. (2006). Cluster analysis in lipid biomarker studies: A case of the Clyde Sea. *Sains Malaysiana*, *35*, 41–47.

Alvarez, L. W., Alvarez, W., Asaro, F., & Michel, H. V. (1980). Experimental results and theoretical interpretation extraterrestrial cause for the Cretaceous-Tertiary extinction. *Science*, *208*(4448), 1095–1108. https://doi.org/10.1126/science.208.4448.1095

Artemieva, N., & Morgan, J. (2009). Modeling the formation of the K-Pg boundary layer. *Icarus*, *201*(2), 768–780. https://doi.org/10.1016/j.icarus.2009.01.021

Berggren, W. A., & Pearson, P. N. (2005). A revised tropical to subtropical Paleocene planktonic foraminiferal zonation. *Journal of Foraminiferal Research*, *35*(4), 279–298. https://doi.org/10.2113/35.4.279

Birch, H., Schmidt, D. N., Coxall, H. K., Kroon, D., & Ridgwell, A. (2021). Ecosystem function after the K/Pg extinction: Decoupling of marine carbon pump and diversity. *Proceedings of the Royal Society B: Biological Sciences*, *288*, 1953. https://doi.org/10.1098/rspb.2021.0863

Birch, H. S., Coxall, H. K., Pearson, P. N., Kroon, D., & Schmidt, D. N. (2016). Partial collapse of the marine carbon pump after the Cretaceous-Paleogene boundary. *Geology*, *44*(4), 287–290. https://doi.org/10.1130/G37581.1

Bourbonniere, R. A., & Meyers, P. A. (1996). Sedimentary geolipid records of historical changes in the watersheds and productivities of Lakes Ontario and Erie. *Limnology & Oceanography*, *41*(2), 352–359. https://doi.org/10.4319/lo.1996.41.2.0352

Bown, P. R., Lees, J. A., & Young, J. R. (2004). Calcareous nannoplankton evolution and diversity through time. Coccolithophores (pp. 481–508). https://doi.org/10.1007/978-3-662-06278-4_18

Bralower, T. J., Cosmidis, J., Heaney, P. J., Kump, L. R., Morgan, J. V., Harper, D. T., et al. (2020). Origin of a global carbonate layer deposited in the aftermath of the Cretaceous-Paleogene boundary impact. *Earth and Planetary Science Letters*, *548*, 116476. https://doi.org/10.1016/j.epsl.2020.116476

Brinkhuis, H., & Leereveld, H. (1988). Dinoflagelate cyst from the Cretaceous/Tertiary boundary sequence of el Kef, Northwest Tunisia. *Review of Palaeobotany and Palynology*, *56*(1–2), 5–19. https://doi.org/10.1016/0034-6667(88)90071-1

Calvert, S. E., & Pedersen, T. F. (1993). Geochemistry of Recent oxic and anoxic marine sediments: Implications for the geological record. *Marine Geology*, *113*(1–2), 67–88. https://doi.org/10.1016/0025-3227(93)90150-t

Carmichael, S. K., Waters, J. A., Königshof, P., Suttner, T. J., & Kido, E. (2019). Paleogeography and paleoenvironments of the Late Devonian Kellwasser event: A review of its sedimentological and geochemical expression. *Global and Planetary Change*, *183*, 102984. https://doi.org/10.1016/j.gloplacha.2019.102984

Carrie, R. H., Mitchell, L., & Black, K. D. (1998). Fatty acids in surface sediment at the Hebridean shelf edge, west of Scotland. *Organic Geochemistry*, *29*(5–7), 1583–1593. https://doi.org/10.1016/S0146-6380(98)00160-0

Cranwell, P. A., Eglinton, G., & Robinson, N. (1987). Lipids of aquatic organisms as potential contributors to lacustrine sediments-II. *Organic Geochemistry*, *11*(6), 513–527. https://doi.org/10.1016/0146-6380(87)90007-6

Dean, R. A., & Whitehead, E. V. (1961). The occurrence of Phytane in petroleum. *Tetrahedron Letters*, *21*, 768–770. https://doi.org/10.1016/s0040-4039(01)99264-0

De Lange, G. J., Van der Sloot, H. A., & Wijkstra, J. (1987). Implications of the diagenetic mobility of Ir for the interpretation of the anomaly at the K/T boundary. *Geological Society Special Publications*, *31*, 147–165.

DePalma, R. A., Smit, J., Burnham, D. A., Kuiper, K., Manning, P. L., Oleinik, A., et al. (2019). A seismically induced onshore surge deposit at the KPg boundary, North Dakota. *Proceedings of the National Academy of Sciences*, *116*(17), 8190–8199. https://doi.org/10.1073/pnas.1817407116

D'Hondt, S. (2005). Consequences of the Cretaceous/Paleogene Mass extinction for marine ecosystems. *Annual Review of Ecology, Evolution and Systematics*, *36*(1), 295–317. https://doi.org/10.1146/annurev.ecolsys.35.021103.105715

Eglinton, G., & Clavin, M. (1967). Certain rocks as much as three billion years old have been found to contain organic compounds. What these compounds are and how they may have originated in living matter is under active study. *Scientific American*, *216*(1), 32–43. https://doi.org/10.1038/scientificamerican0167-32

Eglinton, G., & Hamilton, R. J. (1967). Leaf Epicuticular Waxes. *Science*, *156*(3780), 1322–1335. https://doi.org/10.1126/science.156.3780.1322

Eglinton, T. I., & Eglinton, G. (2008). Molecular proxies for paleoclimatology. *Earth and Planetary Science Letters*, *275*(1–2), 1–16. https://doi.org/10.1016/j.epsl.2008.07.012

Esmeray-Senlet, S., Wright, J. D., Olsson, R. K., Miller, K. G., Browning, J. V., & Quan, T. M. (2015). The Cretaceous/Paleogene mass extinction. *Paleoceanography*, *30*(6), 718–738. https://doi.org/10.1002/2014PA002724.Received

Galeotti, S., Brinkhuis, H., & Huber, M. (2004). Records of post-Cretaceous-Tertiary boundary millennial-scale cooling from the western Tethys: A smoking gun for the impact-winter hypothesis? *Geology*, *32*(6), 529–532. https://doi.org/10.1130/G20439.1

Gao, C., Ruan, X., Zhang, Y. G., Yang, H., Xiao, X., Lü, X., et al. (2023). Biomarker evidence of the water mass structure and primary productivity changes in the Chukchi Sea over the past 70 years. *Frontiers in Marine Science*, *10*, 1077656. https://doi.org/10.3389/fmars.2023.1077656

Gilabert, V., Batenburg, S. J., Arenillas, I., & Arz, J. A. (2021). Contribution of orbital forcing and Deccan volcanism to global climatic and biotic changes across the Cretaceous-Paleogene boundary at Zumaia, Spain. *Geology*, *49*, 1–5. https://doi.org/10.1130/G49214.1/5393375/g49214.pdf

Gulick, S. P. S., Bralower, T. J., Ormö, J., Hall, B., Grice, K., Schaefer, B., et al. (2019). The first day of the Cenozoic. *Proceedings of the National Academy of Sciences of the United States of America*, *116*(39), 19342–19351. https://doi.org/10.1073/pnas.1909479116

Habib, D., Moshkovitz, S., & Kramer, C. (1992). Dinoflagellate change and calcareous nannofossil response to sea-level in Cretaceous-Tertiary boundary sections. *Geology*, *20*(2), 165–168. https://doi.org/10.1130/0091-7613(1992)020<0165:dacnrt>2.3.co;2

Handley, L., Crouch, E. M., & Pancost, R. D. (2011). A New Zealand record of sea level rise and environmental change during the Paleocene-Eocene thermal maximum. *Palaeogeography, Palaeoclimatology, Palaeoecology*, *305*(1–4), 185–200. https://doi.org/10.1016/j.palaeo.2011.03.001

Handley, L., Talbot, H. M., Cooke, M. P., Anderson, K. E., & Wagner, T. (2010). Bacteriohopanepolyols as tracers for continental and marine organic matter supply and phases of enhanced nitrogen cycling on the late Quaternary Congo deep sea fan. *Organic Geochemistry*, *41*(9), 910–914. https://doi.org/10.1016/j.orggeochem.2010.04.016

Hart, M. B., Harries, J. J., & Cárdenas, A. L. (2013). The Cretaceous/Paleogene boundary events in the Gulf Coast: Comparisons between Alabama and Texas. *Gulf Coast Association of Geological Societies Transactions*, *63*, 235–255.

Henehan, M. J., Ridgwell, A., Thomas, E., Zhang, S. G., Alegret, L., Schmidt, D. N., et al. (2019). Rapid ocean acidification and protracted Earth system recovery followed the end-Cretaceous Chicxulub impact. *Proceedings of the National Academy of Sciences of the United States of America*, *116*(45), 22500–22504. https://doi.org/10.1073/pnas.1905989116

Hildebrand, A. R., Penfield, G. T., Kring, D. A., Pilkington, M. A., Camargo, Z. A., Jacobsen, S. B., & Boynton, W. V. (1991). Chicxulub Crater: A possible Cretaceous/Tertiary boundary impact crater on the Yucatán Peninsula, Mexico. *Geology*, *19*(9), 867. https://doi.org/10.1130/0091-7613(1991)019<0867:CCAPCT>2.3.CO;2

Hollingsworth, E. H., Elling, F. J., Badger, M. P. S., Pancost, R. D., Dickson, A. J., Rees-Owen, R. L., et al. (2024). Spatial and Temporal patterns in petrogenic organic carbon Mobilization during the paleocene-Eocene thermal maximum. *Paleoceanography and Paleoclimatology*, *39*(2), 1–20. https://doi.org/10.1029/2023PA004773

Hopmans, E. C., Weijers, J. W. H., Schefuß, E., Herfort, L., Sinninghe Damsté, J. S., & Schouten, S. (2004). A novel proxy for terrestrial organic matter in sediments based on branched and isoprenoid tetraether lipids. *Earth and Planetary Science Letters*, *224*(1–2), 107–116. https://doi.org/10.1016/j.epsl.2004.05.012

Huang, W. Y., & Meinschew, W. G. (1979). Sterols as ecological indicators. *Geochimica et Cosmochimica Acta*, *43*(5), 739–745. https://doi.org/10.1016/0016-7037(79)90257-6

Hull, P. M., Bornemann, A., Penman, D. E., Henehan, M. J., Norris, R. D., Wilson, P. A., et al. (2020). On impact and volcanism across the Cretaceous-Paleogene boundary. *Science*, *367*(6475), 266–272. https://doi.org/10.1126/science.aay5055

Hull, P. M., & Norris, R. D. (2011). Diverse patterns of ocean export productivity change across the Cretaceous-Paleogene boundary: New insights from biogenic barium. *Paleoceanography*, *26*(3), PA3205. https://doi.org/10.1029/2010PA002082

Irizarry, K. M., Witts, J. D., Garb, M., Rashkova, A., Landman, N. H., & Patzkowsky, M. E. (2023). Faunal and stratigraphic analysis of the basal Cretaceous-Paleogene (K-Pg) boundary event deposits, Brazos River, Texas, USA. *Palaeogeography, Palaeoclimatology, Palaeoecology*, *610*, 111334. https://doi.org/10.1016/j.palaeo.2022.111334

Junium, C. K., Zerkle, A. L., Witts, J. D., Ivany, L. C., Yancey, T. E., Liu, C., & Claire, M. W. (2022). Massive perturbations to atmospheric sulfur in the aftermath of the Chicxulub impact. https://doi.org/10.1073/pnas

Kaiho, K., Oshima, N., Adachi, K., Adachi, Y., Mizukami, T., Fujibayashi, M., & Saito, R. (2016). Global climate change driven by soot at the K-Pg boundary as the cause of the mass extinction. *Scientific Reports*, *6*(1), 28427. https://doi.org/10.1038/srep28427

Kinsland, G. L., Egedahl, K., Strong, M. A., & Ivy, R. (2021). Chicxulub impact tsunami megaripples in the subsurface of Louisiana: Imaged in petroleum industry seismic data. *Earth and Planetary Science Letters*, *570*, 117063. https://doi.org/10.1016/j.epsl.2021.117063

Kominz, M. A., Browning, J. V., Miller, K. G., Sugarman, P. J., Mizintseva, S., & Scotese, C. R. (2008). Late cretaceous to Miocene sea-level estimates from the New Jersey and Delaware Coastal Plain coreholes: An error analysis. *Basin Research*, *20*(2), 211–226. https://doi.org/10.1111/j.1365-2117.2008.00354.x

Kring, D. A. (2007). The Chicxulub impact event and its environmental consequences at the Cretaceous-Tertiary boundary. *Palaeogeography, Palaeoclimatology, Palaeoecology*, *255*(1–2), 4–21. https://doi.org/10.1016/j.palaeo.2007.02.037

Kvenvolden, K. A. (1967). Normal fatty acids in sediments. *J Am Oil Chem Soc*, *44*(11), 628–636. https://doi.org/10.1007/BF02680031

Landman, N. H., Johnson, R. O., & Edwards, L. E. (2004). Cephalops from the Cretaceous/Tertiary boundary interval on the Atlantic coastal plain, with a description of the highest ammonite zones in North America. Part 2. Northeastern Monmouth County, New Jersey. *Museum of Natural History*, *287*, 1–107. https://doi.org/10.1206/0003

Larina, E., Garb, M., Landman, N., Dastas, N., Thibault, N., Edwards, L., et al. (2016). Upper Maastrichtian ammonite biostratigraphy of the Gulf Coastal Plain (Mississippi Embayment, southern USA). *Cretaceous Research*, *60*, 128–151. https://doi.org/10.1016/j.cretres.2015.11.010

Li, S., Li, H., Tang, T., & Wang, S. (2024). The Ballast effect of terrigenous Lithogenic particles from rivers and its influence on POC Fluxes in the ocean. *Global Biogeochemical Cycles*, *38*(5), e2024GB008155. https://doi.org/10.1029/2024GB008155

Lowery, C. M., Bown, P. R., Fraass, A. J., & Hull, P. M. (2020). Ecological response of Plankton to environmental change: Thresholds for extinction Christopher. *Annual Review of Earth and Planetary Sciences*, *48*, 16.1–16.27. https://doi.org/10.1146/annurev-earth-081619-052818

Lowery, C. M., & Bralower, T. J. (2022). Elevated post K-Pg export productivity in the Gulf of Mexico and Caribbean. *Paleoceanography and Paleoclimatology*, *37*(9), e2021PA004400. https://doi.org/10.1029/2021PA004400

Lowery, C. M., Bralower, T. J., Owens, J. D., Rodríguez-Tovar, F. J., Jones, H., Smit, J., et al. (2018). Rapid recovery of life at ground zero of the end-Cretaceous mass extinction. *Nature*, *558*(7709), 288–291. https://doi.org/10.1038/s41586-018-0163-6

Lowery, C. M., Jones, H. L., Bralower, T. J., Perez Cruz, L., Gebhardt, C., Whalen, M. T., et al. (2021). Early Paleocene Paleoceanography and export productivity in the Chicxulub crater. *Paleoceanography and Paleoclimatology*, *36*(11), e2021PA004241. https://doi.org/10.1029/2021PA004241

Lowery, C. M., Leckie, R. M., Bryant, R., Elderbak, K., Parker, A., Polyak, D. E., et al. (2018). The Late Cretaceous Western Interior Seaway as a model for oxygenation change in epicontinental restricted basins. *Earth-Science Reviews*, *177*, 545–564. https://doi.org/10.1016/j.earscirev.2017.12.001

Lyons, S. L., Baczynski, A. A., Babila, T. L., Bralower, T. J., Hajek, E. A., Kump, L. R., et al. (2019). Palaeocene–Eocene Thermal Maximum prolonged by fossil carbon oxidation. *Nature Geoscience*, *12*(1), 54–60. https://doi.org/10.1038/s41561-018-0277-3

Lyons, S. L., Karp, A. T., Bralower, T. J., Grice, K., Schaefer, B., Gulick, S. P. S., et al. (2020). Organic matter from the Chicxulub crater exacerbated the K-Pg impact winter. *Proceedings of the National Academy of Sciences of the United States of America*, *117*(41), 25327–25334. https://doi.org/10.1073/pnas.2004596117

Mackenzie, A. S., Patience, R. L., Maxwell, J. R., Vandenbroucke, M., & Durand, B. (1980). Molecular parameters of maturation in the Toarcian shales, Paris basin, France—I. Changes in the configurations of acyclic isoprenoid alkanes, steranes and triterpanes. *Geochimica et Cosmochimica Acta*, *44*(11), 1709–1721. https://doi.org/10.1016/0016-7037(80)90222-7

MacLeod, K. G., Quinton, P. C., Sepúlveda, J., & Negra, M. H. (2018). Postimpact earliest Paleogene warming shown by fish debris oxygen isotopes (El Kef, Tunisia). *Science*, *360*(6396), 1467–1469. https://doi.org/10.1126/science.aap8525

Macleod, N., & Keller, G. (1991). Hiatus distributions and mass extinctions at the Cretaceous/Tertiary boundary. *Geology*, *19*(5), 497–501. https://doi.org/10.1130/0091-7613(1991)019<0497:HDAMEA>2.3.CO

McLachlan, S. M. S., & Pospelova, V. (2021). Calcareous dinoflagellate cyst distribution across the K/Pg boundary at DSDP site 577, Shatsky Rise, western North Pacific Ocean. *Marine Micropaleontology*, *168*, 102057. https://doi.org/10.1016/j.marmicro.2021.102057

Miller, K. G., Kominz, M. A., Browning, J. V., Wright, J. D., Mountain, G. S., Katz, M. E., et al. (2005). The Phanerozoic record of global sea-level change. *Science*, *310*(5752), 1293–1298. https://doi.org/10.1126/science.1116412

Mizukami, T., Kaiho, K., & Oba, M. (2013). Significant changes in land vegetation and oceanic redox across the Cretaceous/Paleogene boundary. *Palaeogeography, Palaeoclimatology, Palaeoecology*, *369*, 41–47. https://doi.org/10.1016/j.palaeo.2012.09.020

Mizukami, T., Kaiho, K., & Oba, M. (2014). A spike of woody plant biomarkers in the deep-sea iridium layer at the Cretaceous/Paleogene boundary. *Palaeogeography, Palaeoclimatology, Palaeoecology*, *412*, 241–248. https://doi.org/10.1016/j.palaeo.2014.07.041

Molina, E., Alegret, L., Arenillas, I., & Arz, J. A. (2005). The cretaceous/paleogene boundary at the Agost section revisited: Paleoenvironmental reconstruction and mass extinction pattern. *Journal of Iberian Geology*, *31*, 135–148.

Morford, J. L., & Emerson, S. (1999). The geochemistry of redox sensitive trace metals in sediments. *Geochimica et Cosmochimica Acta*, *63*(11–12), 1735–1750. https://doi.org/10.1016/S0016-7037(99)00126-X

Morgan, J., Artemieva, N., & Goldin, T. (2013). Revisiting wildfires at the K-Pg boundary. *Journal of Geophysical Research: Biogeosciences*, *118*(4), 1508–1520. https://doi.org/10.1002/2013JG002428

Morgan, J., Warner, M., Chicxulub Working Group, T., Brittan, J., Buffler, R., Camargo, A., et al. (1997). Size and morphology of the Chicxulub impact crater. *Nature*, *390*(6659), 472–476. https://doi.org/10.1038/37291

Morgan, J. V., Bralower, T. J., Brugger, J., & Wünnemann, K. (2022). The Chicxulub impact and its environmental consequences. *Nature Reviews Earth & Environment*, *3*(5), 338–354. https://doi.org/10.1038/s43017-022-00283-y

Naafs, B. D. A., McCormick, D., Inglis, G. N., & Pancost, R. D. (2018). Archaeal and bacterial H-GDGTs are abundant in peat and their relative abundance is positively correlated with temperature. *Geochimica et Cosmochimica Acta*, *227*, 156–170. https://doi.org/10.1016/j.gca.2018.02.025

Naujokaitytė, J., Garb, M. P., Thibault, N., Brophy, S. K., Landman, N. H., Witts, J. D., et al. (2021). Milankovitch cyclicity in the latest cretaceous of the Gulf Coastal Plain, USA. *Sedimentary Geology*, *421*, 105954. https://doi.org/10.1016/j.sedgeo.2021.105954

O'Connor, L. K., Crampton-Flood, E. D., Jerrett, R. M., Price, G. D., Naafs, B. D. A., Pancost, R. D., et al. (2023). Steady decline in mean annual air temperatures in the first 30 k.y. after the Cretaceous-Paleogene boundary. *Geology*, *51*(5), 486–490. https://doi.org/10.1130/G50588.1

Ohno, S., Kadono, T., Kurosawa, K., Hamura, T., Sakaiya, T., Shigemori, K., et al. (2014). Production of sulphate-rich vapour during the Chicxulub impact and implications for ocean acidification. *Nature Geoscience*, *7*(4), 279–282. https://doi.org/10.1038/ngeo2095

Olsson, R. K., Liu, C., & Van Fossen, M. (1996). The Cretaceous-Tertiary catastrophic event at Millers Ferry, Alabama. *Special Papers Geological Society of America*, *307*, 263–277. https://doi.org/10.1130/0-8137-2307-8.263

Ourisson, G., Albrecht, P., & Rohmer, M. (1979). The Hopanoids: Palaeochemistry and biochemistry of a group of natural products. *Pure and Applied Chemistry*, *51*(4), 709–729. https://doi.org/10.1351/pac197951040709

Pälike, H. (2013). Impact and extinction. *Science*, *339*(6120), 655–656. https://doi.org/10.1126/science.1233948

Peryt, D., Alegret, L., & Molina, E. (2002). The Cretaceous/Palaeogene (K/P) boundary at Aïn Settara, Tunisia: Restructuring of benthic foraminiferal assemblages. *Terra Nova*, *14*(2), 101–107. https://doi.org/10.1046/j.1365-3121.2002.00394.x

Peters, K. E., & Moldowan, J. M. (1991). Effects of source, thermal maturity, and biodegradation on the distribution and isomerization of homohopanes in petroleum. *Organic Geochemistry*, *17*(1), 47–61. https://doi.org/10.1016/0146-6380(91)90039-M

Peters, K. E., Peters, K. E., Walters, C. C., & Moldowan, J. M. (2005). *The biomarker guide*. Cambridge University Press.

Raup, D. M., & Sepkoski, J. J. (1982). Mass extinctions in the marine fossil record. *Science*, *215*(4539), 1501–1503. https://doi.org/10.1126/science.215.4539.1501

Renne, P. R., Sprain, C. J., Richards, M. A., Self, S., Vanderkluysen, L., & Pande, K. (2015). Possibly induced by impact. *Science*, *350*(6256), 76–78. https://doi.org/10.1126/science.aac7549

Rieley, G., Collier, R. J., Jones, D. M., Eglinton, G., Eakint, P. A., & Fallickt, A. E. (1991). Sources of sedimentary lipids deduced from stable carbon- isotope analyses of individual compounds. *Nature*, *352*(6334), 425–427. https://doi.org/10.1038/352425a0

Rodríguez-Tovar, F. J., Lowery, C. M., Bralower, T. J., Gulick, S. P. S., & Jones, H. L. (2020). Rapid macrobenthic diversification and stabilization after the end-Cretaceous mass extinction event. *Geology*, *48*(11), 1048–1052. https://doi.org/10.1130/g47589.1

Rontani, J. F., & Volkman, J. K. (2003). Phytol degradation products as biogeochemical tracers in aquatic environments. *Organic Geochemistry*, *34*, 1–35. https://doi.org/10.1016/s0146-6380(02)00185-7

Rosenberg, Y. O., Ashckenazi-Polivoda, S., Abramovich, S., Thibault, N., Chin, S., Feinstein, S., et al. (2021). Resilience of primary and export productivity in a eutrophic ecosystem following the Cretaceous-Paleogene mass extinction. *Global and Planetary Change*, *196*, 103371. https://doi.org/10.1016/j.gloplacha.2020.103371

Sanford, J. C., Snedden, J. W., & Gulick, S. P. S. (2016). The Cretaceous-Paleogene boundary deposit in the Gulf of Mexico: Large oceanic basin response to the Chicxulub impact. *Journal of Geophysical Research*, *121*(3), 1240–1261. https://doi.org/10.1002/2015JB012615

Santa Catharina, A., Kneller, B. C., Marques, J. C., McArthur, A. D., Cevallos-Ferriz, S. R. S., Theurer, T., et al. (2022). Timing and causes of forest fire at the K–Pg boundary. *Scientific Reports*, *12*(1), 13006. https://doi.org/10.1038/s41598-022-17292-y

Savrda, C. E. (2018). Revisiting the origins of Clayton sand bodies at the K-Pg transition, Moscow Landing, Western Alabama: Stratigraphic relations, sedimentology, and ichnology. *PALAIOS*, *33*(12), 555–567. https://doi.org/10.2110/palo.2018.086

Scasso, R. A., Prámparo, M. B., Vellekoop, J., Franzosi, C., Castro, L. N., & Sinninghe Damsté, J. S. (2020). A high-resolution record of environmental changes from a Cretaceous-Paleogene section of Seymour Island, Antarctica. *Palaeogeography, Palaeoclimatology, Palaeoecology*, *555*, 109844. https://doi.org/10.1016/j.palaeo.2020.109844

Schaefer, B., Grice, K., Coolen, M. J. L., Summons, R. E., Cui, X. X., Bauersachs, T., et al. (2020). Microbial life in the nascent chicxulub crater. *Geology*, *48*(4), 1–5. https://doi.org/10.3997/2214-4609.201902850

Schneider, H., Gelpi, E., Bennett, E. O., & Oró, J. (1970). Fatty acids of geochemical significance in microscopic algae. *Phytochemistry*, *9*(3), 613–617. https://doi.org/10.1016/S0031-9422(00)85701-5

Schoene, B., Samperton, K. M., Eddy, M. P., Keller, G., Adatte, T., Bowring, S. A., et al. (2015). U-Pb geochronology of the Deccan Traps and relation to the end-Cretaceous mass extinction. *Science*, *347*(6218), 182–184. https://doi.org/10.1126/science.aaa0118

Schoene, B. L., Eddy, M. P., Samperton, K. M., Keller, C. B., Keller, G., Adatte, T., & Khadri, S. F. R. (2019). U-Pb constraints on pulsed eruption of the Deccan Traps across the end-Cretaceous mass extinction. *Science*, *363*(6429), 862–866. https://doi.org/10.1126/science.aau2422

Schouten, S., Hopmans, E. C., & Sinninghe Damsté, J. S. (2013). The organic geochemistry of glycerol dialkyl glycerol tetraether lipids: A review. *Organic Geochemistry*, *54*, 19–61. https://doi.org/10.1016/j.orggeochem.2012.09.006

Schouten, S., Ossebaar, J., Brummer, G. J., Elderfield, H., & Sinninghe Damsté, J. S. (2007). Transport of terrestrial organic matter to the deep North Atlantic Ocean by ice rafting. *Organic Geochemistry*, *38*(7), 1161–1168. https://doi.org/10.1016/j.orggeochem.2007.02.012

Schulte, P., Alegret, L., Arenillas, I., Arz, J. A., Barton, P. J., Bown, P. R., et al. (2010). The chicxulub asteroid impact and mass extinction at the cretaceous-paleogene boundary. *Science*, *327*(5970), 1214–1218. https://doi.org/10.1126/science.1177265

Schulte, P., Speijer, R., Mai, H., & Kontny, A. (2006). The Cretaceous-Paleogene (K-P) boundary at Brazos, Texas: Sequence stratigraphy, depositional events and the Chicxulub impact. *Sedimentary Geology*, *184*(1–2), 77–109. https://doi.org/10.1016/j.sedgeo.2005.09.021

Schulte, P., & Speijer, R. P. (2009). Late Maastrichtian-early paleocene sea level and climate changes in the Antioch Church Core (Alabama, Gulf of Mexico margin, USA): A multi-proxy approach. *Geológica Acta*, *7*, 11–34. https://doi.org/10.1344/105.000000279

Schwark, L., & Empt, P. (2006). Sterane biomarkers as indicators of palaeozoic algal evolution and extinction events. *Palaeogeography, Palaeoclimatology, Palaeoecology*, *240*(1–2), 225–236. https://doi.org/10.1016/j.palaeo.2006.03.050

Seifert, W. K., & Moldowan, J. M. (1980). The effect of thermal stress on source-rock quality as measured by hopane stereochemistry. *Physics and Chemistry of the Earth*, *12*, 229–237. https://doi.org/10.1016/0079-1946(79)90107-1

Senel, C. B., Kaskes, P., Temel, O., Vellekoop, J., Goderis, S., DePalma, R., et al. (2023). Chicxulub impact winter sustained by fine silicate dust. *Nature Geoscience*, *16*(11), 1033–1040. https://doi.org/10.1038/s41561-023-01290-4

Sepúlveda, J., Alegret, L., Thomas, E., Haddad, E., Cao, C., & Summons, R. E. (2019). Stable isotope constraints on marine productivity across the Cretaceous-paleogene mass extinction. *Paleoceanography and Paleoclimatology*, *34*(7), 1195–1217. https://doi.org/10.1029/2018PA003442

Sepúlveda, J., Wendler, J. E., Summons, R. E., & Hinrichs, K.-U. (2009). Rapid Resurgence of marine productivity after the cretaceous-paleogene mass extinction. *Science*, *326*(5949), 129–132. https://doi.org/10.1126/science.1176233

Smit, J. (1999). The global stratigraphy of the Cretaceous-Tertiary boundary impact ejecta. *Annual Review of Earth and Planetary Sciences*, *27*(1), 75–113. https://doi.org/10.1146/annurev.earth.27.1.75

Smit, J., & Hertogen, J. (1980). An extraterrestrial event at the Cretaceous-Tertiary boundary. *Nature*, *285*(5762), 198–200. https://doi.org/10.1038/285198a0

Smit, J., Roep, T. B., Alvarez, W., Montanari, A., Claeys, P., Grajales-Nishimura, J. M., & Bermudez, J. (1996). Coarse-grained, clastic sandstone complex at the K/T boundary around the Gulf of Mexico: Deposition by tsunami waves induced by the Chicxulub impact? *Geological Society of America*, *307*, 151–182.

Snedden, J. W., Lowery, C. M., & Lawton, T. F. (2024). The End of the Cretaceous: Depositional paleogeographic reconstruction of the Gulf of Mexico and adjacent areas just prior to the Chicxulub impact. *Geological Society, London, Special Publications*, *545*(1), SP545. https://doi.org/10.1144/sp545-2023-51

Sosa-Montes de Oca, C. (2024). Intense changes in the main source of organic carbon to the ocean following the Cretaceous-Paleogene boundary [Dataset]. *OSF*. https://doi.org/10.17605/OSF.IO/ZMA9G

Sosa-Montes de Oca, C., de Lange, G. J., Martínez-Ruiz, F., Ortega-Huertas, M., & Rodríguez-Tovar, F. J. (2020). Microscale trace-element distribution across the Cretaceous/Palaeogene ejecta layer at the Agost section: Constraining the recovery of pre-impact conditions. *Chemical Geology*, *533*, 119431. https://doi.org/10.1016/j.chemgeo.2019.119431

Sosa-Montes de Oca, C., de Lange, G. J., Martínez-Ruiz, F., & Rodríguez-Tovar, F. J. (2018a). Application of laser ablation-ICP-MS to determine high-resolution elemental profiles across the Cretaceous/Paleogene boundary at Agost (Spain). *Palaeogeography, Palaeoclimatology, Palaeoecology*, *497*, 128–138. https://doi.org/10.1016/j.palaeo.2018.02.012

Sosa-Montes de Oca, C., de Lange, G. J., Martínez-Ruiz, F., & Rodríguez-Tovar, F. J. (2018b). High-resolution data from laser ablation-ICP-MS and by ICP-OES analyses at the cretaceous/paleogene boundary section at Agost (SE Spain). *Data in Brief*, *18*, 1900–1906. https://doi.org/10.1016/j.dib.2018.04.118

Sosa-Montes de Oca, C., Martínez-Ruiz, F., & Rodríguez-Tovar, F. J. (2013). Bottom-water conditions in a marine basin after the Cretaceous-Paleogene impact event: Timing the recovery of oxygen levels and productivity. *PLoS One*, *8*(12), e82242. https://doi.org/10.1371/journal.pone.0082242

Sosa-Montes de Oca, C., Rodrigo-Gámiz, M., Martínez-Ruiz, F., Rodríguez-Tovar, F. J., Castro, J. M., Quijano, M. L., & Pancost, R. D. (2021). Minor changes in biomarker assemblages in the aftermath of the Cretaceous-Paleogene mass extinction event at the Agost distal section (Spain). *Palaeogeography, Palaeoclimatology, Palaeoecology*, *569*, 110310. https://doi.org/10.1016/j.palaeo.2021.110310

Sosa-Montes de Oca, C., Taylor, K. W. R., Hollis, C. J., Huang, Y., & Pancost, R. D. (2023). Variation in organic matter across the Cretaceous-Paleogene boundary in New Zealand supports the "Living Ocean" model of biotic recovery. *Global and Planetary Change*, *220*, 104025. https://doi.org/10.1016/j.gloplacha.2022.104025

Speijer, R. P., Pälike, H., Hollis, C. J., Hooker, J. J., & Ogg, J. G. (2020). The paleogene period. In *Geologic time Scale 2020* (pp. 1087–1140). Elsevier. https://doi.org/10.1016/B978-0-12-824360-2.00028-0

Sprain, C. J., Renne, P. R., Clemens, W. A., & Wilson, G. P. (2018). Calibration of chron C29r: New high-precision geochronologic and paleomagnetic constraints from the Hell Creek region, Montana. *Bulletin of the Geological Society of America*, *130*(9–10), 1615–1644. https://doi.org/10.1130/B31890.1

Swisher, C. C., Grajales-Nishimura, J. M., Montanari, A., Margolis, S. V., Claeys, P., Alvarez, W., et al. (1992). Coeval $^{40}Ar/^{39}Ar$ ages of 65.0 million years ago from Chicxulub crater melt rock and Cretaceous-Tertiary boundary tektites. *Science*, *257*(5072), 954–958. https://doi.org/10.1126/science.257.5072.954

Taylor, K. W. R., Willumsen, P. S., Hollis, C. J., & Pancost, R. D. (2018). South Pacific evidence for the long-term climate impact of the Cretaceous/Paleogene boundary event. *Earth-Science Reviews*, *179*, 287–302. https://doi.org/10.1016/j.earscirev.2018.02.012

Toulmin, L. D. (1977). *Stratigraphic distribution of Paleocene and Eocene fossils in the eastern Gulf Coast region*. Geological Survey of Alabama, Geologic Division.

Tribovillard, N., Algeo, T. J., Lyons, T., & Riboulleau, A. (2006). Trace metals as paleoredox and paleoproductivity proxies: An update. *Chemical Geology*, *232*(1–2), 12–32. https://doi.org/10.1016/j.chemgeo.2006.02.012

Van der Weijden, C. H. (2002). Pitfalls of normalization of marine geochemical data using a common divisor. *Marine Geology*, *184*(3–4), 167–187. https://doi.org/10.1016/s0025-3227(01)00297-3

Vellekoop, J., Esmeray-Senlet, S., Miller, K. G., Browning, J. V., Sluijs, A., van de Schootbrugge, B., et al. (2016). Evidence for Cretaceous-Paleogene boundary bolide "impact winter" conditions from New Jersey, USA. *Geology*, *44*(8), 619–622. https://doi.org/10.1130/G37961.1

Vellekoop, J., Holwerda, F., Prámparo, M. B., Willmott, V., Schouten, S., Cúneo, N. R., et al. (2017). Climate and sea-level changes across a shallow marine Cretaceous–Palaeogene boundary succession in Patagonia, Argentina. *Palaeontology*, *60*(4), 519–534. https://doi.org/10.1111/pala.12297

Vellekoop, J., Sluijs, A., Smit, J., Schouten, S., Weijers, J. W. H., Sinninghe Damste, J. S., & Brinkhuis, H. (2014). Rapid short-term cooling following the Chicxulub impact at the Cretaceous-Paleogene boundary. *Proceedings of the National Academy of Sciences of the United States of America*, *111*(21), 1–5. https://doi.org/10.1073/pnas.1319253111

Vellekoop, J., Smit, J., van de Schootbrugge, B., Weijers, J. W. H., Galeotti, S., Sinninghe Damste, J. S., & Brinkhuis, H. (2015). Palynological evidence for prolonged cooling along the Tunisian continental shelf following the K-Pg boundary impact. *Palaeogeography, Palaeoclimatology, Palaeoecology*, *426*, 216–228. https://doi.org/10.1016/j.palaeo.2015.03.021

Vellekoop, J., Woelders, L., van Helmond, N. A. G. M., Galeotti, S., Smit, J., Slomp, C. P., et al. (2018). Shelf hypoxia in response to global warming after the Cretaceous-Paleogene boundary impact. *Geology*, *46*(8), 683–686. https://doi.org/10.1130/G45000.1

Wade, B. S., Pearson, P. N., Berggren, W. A., & Pälike, H. (2011). Review and revision of Cenozoic tropical planktonic foraminiferal biostratigraphy and calibration to the geomagnetic polarity and astronomical time scale. *Earth-Science Reviews*, *104*(1–3), 111–142. https://doi.org/10.1016/j.earscirev.2010.09.003

Weijers, J. W. H., Schouten, S., Spaargaren, O. C., & Sinninghe Damsté, J. S. (2006). Occurrence and distribution of tetraether membrane lipids in soils: Implications for the use of the TEX86 proxy and the BIT index. *Organic Geochemistry*, *37*(12), 1680–1693. https://doi.org/10.1016/j.orggeochem.2006.07.018

Witts, J. D., Landman, N. H., Garb, M. P., Irizarry, K. M., Larina, E., Thibault, N., et al. (2021). Cephalopods from the cretaceous-paleogene (K-Pg) boundary interval on the Brazos river, Texas and extinction of ammonites. *American Museum Novitates*, *3964*, 52.

Witts, J. D., Newton, R. J., Mills, B. J. W., Wignall, P. B., Bottrell, S. H., Hall, J. L. O., et al. (2018). The impact of the Cretaceous–Paleogene (K–Pg) mass extinction event on the global sulfur cycle: Evidence from Seymour Island, Antarctica. *Geochimica et Cosmochimica Acta*, *230*, 17–45. https://doi.org/10.1016/j.gca.2018.02.037

Xie, S., Pancost, R. D., Wang, Y., Yang, H., Wignall, P. B., Luo, G., et al. (2010). Cyanobacterial blooms tied to volcanism during the 5 m.y. Permo-Triassic biotic crisis. *Geology*, *38*, 447–450. https://doi.org/10.1130/G30769.1

Zhang, S., Hu, X., Han, Z., Li, J., & Garzanti, E. (2018). Climatic and tectonic controls on Cretaceous-Palaeogene sea-level changes recorded in the Tarim epicontinental sea. *Palaeogeography, Palaeoclimatology, Palaeoecology*, *501*, 92–110. https://doi.org/10.1016/j.palaeo.2018.04.008